Solar, Net, and Photosynthetic Radiation

J. Mark Blonquist Jr. and Bruce Bugbee*

Introduction

Shortwave and longwave radiation incident at Earth's surface are the source of available energy that controls key processes, including surface and atmospheric heating, evaporation, sublimation, transpiration, and photosynthesis. Shortwave radiation (approximately 280 to 4000 nm) is emitted by the sun, whereas longwave radiation (approximately 4000 to 100 000 nm) is emitted by molecules in the atmosphere and objects at the surface. There is no universally accepted definition of the cutoff wavelengths for shortwave or longwave radiation, but there is minimal shortwave radiation at wavelengths greater than 3000 nm.

Shortwave and longwave radiation at Earth's surface are spatially and temporally variable due to changes in position of the sun with respect to Earth's surface and changes in atmospheric conditions. Shortwave radiation accounts for a larger proportion of total radiation at the surface, but longwave radiation is a significant contributor. Ultimately, solar radiation is the source of available energy at Earth's surface and within Earth's atmosphere, driving weather and climate, as longwave radiation results from atmospheric and surface heating by shortwave radiation.

Radiation Theory

Radiation is energy transfer in the form of electromagnetic waves. All materials with temperature above absolute zero continuously emit electromagnetic radiation. The intensity and wavelengths of radiation emitted are dependent on temperature, according to Planck's Law, which describes the spectral (wavelength-dependent) distribution of electromagnetic radiation emitted by an object as a function of absolute temperature (T, in units of K) and emissivity (ε_λ):

$$B_\lambda = \frac{2\pi\varepsilon_\lambda hc^2}{\lambda^5\left[e^{\left(\frac{hc}{\lambda kT}\right)}-1\right]} \qquad [1]$$

where B_λ is radiation intensity (energy flux density) (W m^{-2} m^{-1}), h is Planck's constant (6.6261 × 10^{-34} J s), c is speed of light in vacuum (2.9979 × 10^8 m s^{-1}), k is the Boltzmann constant (1.3807 × 10^{-23} J K^{-1}), and λ is wavelength (m). Emissivity (ε_λ, subscript λ denotes wavelength-dependent) is defined as the fraction of black-body emission. A blackbody is an object with an emissivity of one, emitting the maximum amount of radiation for its temperature. Thus, emissivity is the ratio of energy emitted by an object to energy emitted by a blackbody at the same temperature. For most terrestrial surfaces, emissivities are near one.

In addition to being a stream of energy, radiation can also be described and quantified as a stream of elementary particles called photons, which are defined as a single quantum of radiation and can be thought of as discrete energy packets. Thus, radiation can be expressed in units of energy (typically Joules) or quantity (number of photons or often moles of photons). Both units of measurement are important in environmental applications, and the application will determine the appropriate units. For example, energy flux density drives evapotranspiration and photon flux density drives photosynthesis. The relationship between units of energy and units of quantity is:

$$B_\lambda = \frac{n_\lambda hc}{\lambda} \qquad [2]$$

where n_λ is number of photons, and h, c, and λ are as defined for Eq. [1]. When $n_\lambda = 1$, Eq. [2] yields energy content (J) of a single photon. To calculate energy content of a mole of photons (mol), Avogadro's number (6.0221 × 10^{23}) is input for n_λ.

Typically, radiation is measured in terms of flux density, a flux of energy or flux of photons over a unit area (often 1 m^2), where flux is flow of energy or photons per unit time (often 1 s). Typical units for energy flux are power (W = J s^{-1}), and power per unit area (W m^{-2} = J m^{-2} s^{-1}) for energy flux density. Typical units for photon flux are number of photons per unit time (μmol s^{-1}), and number of photons per unit time per unit area (μmol m^{-2} s^{-1}) for photon flux density. Sometimes the single word 'flux' is used to indicate units of time and area in the denominator, rather than just time. To avoid ambiguity, herein flux is defined as energy or quantity per unit time, and flux density is defined as energy or quantity per unit time per unit area.

Integration of Eq. [1] across an infinite wavelength range (λ ranging from 0 to ∞) yields the Stefan–Boltzmann Law, describing total energy flux density (E, in units of W m^{-2}) from an object as a function of absolute temperature:

$$E = \varepsilon \sigma T^4 \qquad [3]$$

where ε is broadband emissivity (effective emissivity for all wavelengths emitted), σ is the Stefan-Boltzmann constant (5.6704 × 10^{-8} W m^{-2} K^{-4}), and T is absolute temperature (K). Differentiation of Eq. [1] with respect to wavelength yields Wien's Displacement Law, relating the wavelength of peak emission (λ_{max}, in units of μm) for a blackbody radiator to absolute temperature:

$$\lambda_{max} = \frac{2898}{T} \qquad [4]$$

In energy units, flux density from all directions incident on a surface of unit area is called incident radiation flux density, or irradiance. Irradiance is often measured on a horizontal surface for the hemispherical field of view above the surface. Irradiance at Earth's surface measured with respect to a horizontal plane is often called global hemispherical irradiance or global irradiance. Total global irradiance at Earth's surface contains shortwave and longwave components.

Shortwave irradiance at Earth's surface is often defined as radiant energy in the 280 to 4000 nm wavelength range, but the cutoff at 4000 nm is somewhat arbitrary, with 4000 nm being an approximation of the point where shortwave and longwave radiation spectra overlap (Fig. 1). Wavelengths shorter than 280 nm are emitted by the sun and are considered shortwave radiation, but are absorbed by Earth's atmosphere (largely by ozone molecules) before reaching the surface. Shortwave radiation at Earth's surface is often subdivided into ultraviolet (UV, 280 to 400 nm), visible (400 to 700 nm), and near infrared (NIR, 700 to 4000 nm) wavelength ranges.

Global shortwave irradiance incident on Earth's surface (SW_i) is made up of direct and diffuse components. Direct irradiance is transmitted through the atmosphere without interacting with air molecules (no absorption or scattering) and is the major contributor to SW_i, approximately 90%, on clear days in the middle of the day. Diffuse irradiance interacts with air molecules and atmospheric constituents (e.g., clouds, aerosols, pollutants) and is scattered or reflected in the direction of Earth's surface. Diffuse irradiance contributes approximately 10% to SW_i on clear days in the middle of the day, but the contribution increases as the solar zenith angle increases. Diffuse irradiance also increases as cloud cover increases and is the only contributor to SW_i on overcast days. A fraction of diffuse irradiance is shortwave radiation reflected by Earth's surface and then scattered back toward the surface by the atmosphere. This component of diffuse irradiance increases as Earth's surface reflectivity increases.

Longwave irradiance at Earth's surface is radiant energy in the thermal infrared (IR) wavelength range, typically defined as wavelengths greater than 4000 nm or 4 μm. Longwave radiation is energy emitted by objects with temperature that is not hot enough to result in shortwave radiation. Calculation of radiant energy emission for the sun and Earth's surface using Eq. [1],
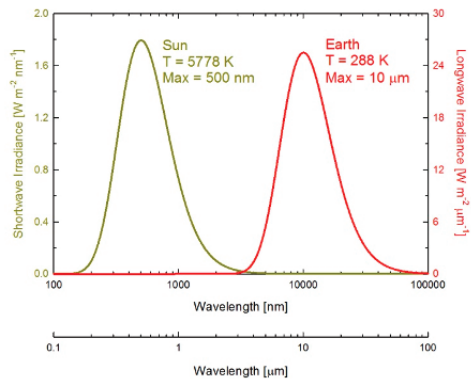
Fig. 1. Wavelength distributions, calculated with Eq. [1] (assuming ε_λ = 1 at all wavelengths for the sun and Earth), for shortwave irradiance incident at the top of Earth's atmosphere (sun was assumed to be a 5778 K blackbody and mean distance between Earth and sun was assumed) and longwave irradiance emitted from Earth (assumed to be a 288 K blackbody). The wavelengths of maximum emission (peaks in the distributions) were calculated with Eq. [4]. There is little overlap between the two distributions (intersection is between 3000 and 4000 nm), allowing for relatively distinct definitions of shortwave and longwave radiation. Note the change in units on the y axis scales for shortwave and longwave irradiance, where shortwave irradiance is per nm and longwave irradiance is per μm.
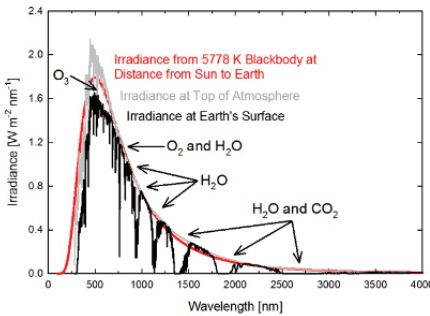
where the distance between Earth and sun was accounted for to yield top of atmosphere shortwave irradiance (extraterrestrial radiation), shows little overlap between the two distributions of wavelengths (Fig. 1). Global longwave irradiance incident on Earth's surface (LW_i) is only diffuse because the air molecules responsible for emitting longwave radiation are relatively evenly distributed in the atmosphere and emit radiation in all directions.

This chapter reviews radiation measurements made at Earth's surface and is divided into three sections, each reviewing a specific measurement common to agricultural applications: Global Shortwave Irradiance, Net Radiation, and Photosynthetically Active Radiation. Each section contains subsections that cover specific topics related to each measurement.

Global Shortwave Irradiance

Shortwave irradiance at the top of Earth's atmosphere on a plane perpendicular to the sun's rays at the mean distance between Earth and the sun is nearly constant, and is often called the solar constant. Traditional values of the solar constant range from 1365 to 1370 W m^{-2}, but data from a recent study indicate it is closer to 1361 W m^{-2} (Kopp and Lean, 2011). The solar constant is not a true constant, but varies with solar cycles (Steinhilber et al., 2009; Vieira et al., 2011). The distance between Earth and the sun varies with time of year, and is at a minimum in January and a maximum in July. Thus, top of atmosphere shortwave irradiance is seasonally variable.

Shortwave irradiance at the top of Earth's atmosphere approximates that calculated with Eq. [1] for a 5778 K blackbody at the mean distance between the sun and Earth, but there are some differences due to absorption and emission by gases in the outermost layer of the sun (Fig. 2). As shortwave radiation passes through Earth's atmosphere it is absorbed, reflected, and scattered by air molecules, clouds, aerosols, and particulate matter (e.g., dust, smoke, pollutants). Thus, shortwave irradiance at Earth's surface is less than top of atmosphere shortwave irradiance, particularly at certain wavelengths where absorption by atmospheric gases (ozone, oxygen, water vapor, carbon dioxide) is strong (Fig. 2). On clear days, 70 to 80% of top of atmosphere shortwave irradiance

Fig. 2. Shortwave irradiance spectra from a 5778 K blackbody at the mean distance between the sun and Earth (calculated from Eq. [1]), at the top of Earth's atmosphere (American Society for Testing and Materials (ASTM) G173–03 Reference Solar Spectral Irradiance, derived from Simple Model of the Atmospheric Radiative Transfer of Sunshine (SMARTS) v. 2.9.2, available at: http://rredc.nrel.gov/solar/spectra/am1.5/ASTMG173/ASTMG173.html, verified 17 July 2016), and at Earth's surface on a clear day (measured on a clear day near solar noon in June in Logan, UT, with an Advanced Spectral Designs model FieldSpec Pro spectroradiometer). Absorption by atmospheric gases [ozone (O_3,) oxygen (O_2,) water vapor (H_2O), carbon dioxide (CO_2)] reduces radiation transmission and causes spectral differences in shortwave irradiance between top of atmosphere and Earth's surface.
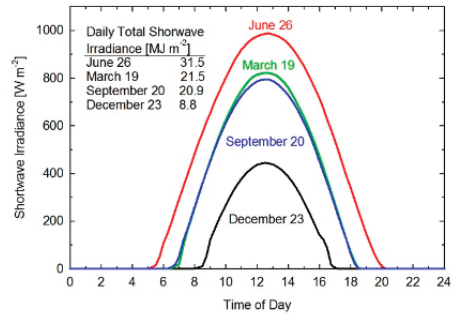
is transmitted to Earth's surface. The rest is absorbed and scattered by gases and particulates in the atmosphere. Shortwave irradiance at Earth's surface is highly variable in space and time, with the largest contributors to variability being time of year and time of day (Fig. 3), and atmospheric water content and degree of cloudiness. A typical value of global shortwave irradiance (SW_i) for a midlatitude location in summer on a clear day near solar noon is 1000 W m^{-2}. High, thin clouds can enhance SW_i by as much as 50% by reflection (Yordanov et al., 2012), whereas thick clouds reduce SW_i to approximately 10%.

Radiometers designed to measure SW_i are called pyranometers. There are two main types

Fig. 3. Seasonal comparison of global shortwave irradiance in Logan, Utah, United States (41.77° N lat. 111.86° W long.), for days near solstices and equinoxes (clear sky days near solstices and equinoxes in 2014 were selected). Global shortwave irradiance was integrated over the course of the day to provide daily totals (energy flux density on a daily time scale) listed in the table.

of pyranometer: blackbody thermopile and silicon-cell. Blackbody thermopile pyranometers use the thermoelectric effect (conversion of a temperature difference between two different metals or alloys to voltage) and silicon-cell pyranometers use the photoelectric effect (electron emission driven by photon absorption in a semiconductor) to generate electrical signals proportional to SW_i.

Blackbody Thermopile Pyranometers

Blackbody thermopile pyranometers use the combination of a glass dome (or two domes), blackbody absorber, and thermopile (multiple thermocouple junctions connected in series) transducer to produce a voltage signal proportional to incident shortwave radiation. Blackbody pyranometers with alternative transducers to thermopiles (e.g., platinum resistance thermometers) have also been built (Beaubien et al., 1998), but they are not commonly used. Voltage output by a thermopile is equal to the temperature difference between sensing (hot) and reference (cold) junctions multiplied by the number of thermocouple junctions in the thermopile and the Seebeck coefficient (thermocouple sensitivity, which is dependent on thermocouple type) of the thermocouples. The sensing junction of the thermopile is thermally bonded to the blackbody absorber and the reference junction of the thermopile is thermally bonded to the sensor housing, which is used as a heat sink. Radiation incident on the blackbody absorber (top surface of the detector plate) heats the detector plate and sensing junction above the internal reference junction, which is shaded from shortwave radiation. Voltage output by the thermopile is proportional to the temperature difference and heat flux between the blackbody surface and internal reference junction, and scales linearly with incident radiation. To minimize errors, heat flux to the absorber should only be from incident shortwave radiation and heat flux away from the absorber should only be via conduction to the thermopile. Heat gain by the blackbody surface not caused by incident shortwave radiation (e.g., absorption of longwave radiation) and heat

loss by the blackbody absorber not caused by conduction to the thermopile (e.g., conduction to sensor housing adjacent to the absorber or convection caused by wind) cause changes in signal unrelated to shortwave irradiance.

Blackbody absorbers are sensitive to both shortwave and longwave radiation, so a filter must be used to block longwave radiation. Glass domes are typically used for this purpose, as transmittance of glass is near 100% and uniformly transmits wavelengths from about 290 to 3000 nm. Quartz domes are also sometimes used, and extend the transmittance range from 200 to 3600 nm. Domes protect the absorber surface from dust and moisture, which reduce absorptivity. Domes also provide an insulative barrier that reduces the influence of wind and thermal gradients on advective and convective heat loss from the absorber. Lower cost instruments have a single dome. Higher cost instruments have two domes, a smaller inner dome covered by a larger outer dome, which further reduce advective and convective heat losses from the absorber. The blackbody absorber should be thermally isolated from other sensor components to minimize conductive heat loss. The absorber is an efficient emitter of longwave radiation, and when exposed to a clear cold sky, the absorber and domes cool via longwave emission. This radiative heat loss, often referred to as a thermal offset (discussed below), varies with sky conditions. It is maximum under clear sky conditions and minimum when the sky is overcast.

Some thermopile pyranometers have black and white receiving surfaces (e.g., Eppley Laboratory model 8–48), where the temperature difference measured by the thermopile is between the black (absorbing) and white (reference) surfaces, rather than a black absorbing surface and internal reference point. The black surface has high shortwave absorptivity and heats up relative to the white surface, which has high shortwave reflectivity. The advantage of this design over a completely black surface is that the black and white surfaces are subject to the same conditions (exposure, wind, and thermal gradients), so a single dome can be used and heat exchange between black and white surfaces via advection and convection is minimal. Thermal offset is also minimized because black and white surfaces are both exposed to the sky. The disadvantage of this type of design is daily and seasonal changes in sun alignment with respect to black and white surfaces. Also, discoloration of the white reference surfaces alters shortwave reflectivity, which changes the calibration.

Silicon-cell Pyranometers

Silicon-cell pyranometers consist of a silicon photodiode mounted behind a diffuser. Silicon is a semiconductor that emits electrons (electrical current) in response to incident photons (radiation) of specific wavelength. The diffuser is designed to provide accurate angular response and is typically made of acrylic with a white colorant added to make it opaque. Some models output short circuit current from the photodiode directly, but in most models manufacturers add a shunt resistor to convert current to voltage. The electrical signal is linearly related to incident radiation within the range of silicon sensitivity. Silicon is generally sensitive to wavelengths from about 350 to 1100 nm. The transmittance of acrylic is fairly uniform across this range (Kerr et al., 1967).

The limited sensitivity of the detector (350 to 1100 nm) means that silicon-cell pyranometers subsample the solar spectrum and must be calibrated to estimate total shortwave irradiance. Changes in sky conditions can change proportions

of SW_i within the silicon-cell sensitivity range. For example, 70 to 80% of SW_i is between 350 and 1100 nm on a clear day (Myers, 2011), and about 90% of SW_i is within this range on an overcast day due to absorption by water vapor at wavelengths greater than 1100 nm (Federer and Tanner, 1965; Kerr et al., 1967). This results in spectral errors for different sky conditions (discussed below). Silicon-cell pyranometers are most accurate in conditions similar to those during calibration (Habte et al., 2014).

While silicon-cell pyranometers have the disadvantage of spectral error, they have the advantage of lower cost, smaller size, and faster response. Fast response can be important for solar power applications (Sengupta et al., 2012), but is not necessarily an advantage for weather and climate measurements. Response time of thermopile pyranometers is determined by thermal mass and thermal conductivity of components, and is typically a few seconds, whereas the response of silicon-cell pyranometers is independent of these factors, and is less than 1 ms. A new blackbody thermopile pyranometer (EKO Instruments model MS-80) has a response time of 0.5 s, resulting largely from a small (low thermal mass) detector.

Pyranometer Classification

Three classes of pyranometers are defined based on performance characteristics and specifications. Two organizations, the World Meteorological Organization (WMO) and the International Organization for Standardization (ISO), have instituted similar classifications (Table 1). The names of the classes in the ISO classification can be confusing because similar names, Second Class and Secondary Standard, are used for classes. The lowest cost blackbody thermopile pyranometers are classified as Moderate Quality (WMO classification) and second class (ISO classification), and price increases as classification increases. Several models of blackbody thermopile pyranometers are available, for example:

Moderate Quality (WMO) or Second Class (ISO): EKO Instruments model MS-602, Hukseflux model LP02, Kipp & Zonen model CMP 3.

Good Quality (WMO) or First Class (ISO): EKO Instruments model MS-402, Hukseflux model SR11, Kipp & Zonen model CMP 6.

High Quality (WMO) or Secondary Standard (ISO): EKO Instruments model MS-802, Eppley Laboratory model SPP, Hukseflux model SR20, Kipp & Zonen model CMP 11.

Specifications for silicon-cell pyranometers (e.g., Apogee Instruments model SP-110, EKO Instruments model ML-01, Kipp & Zonen model SP Lite2, LI-COR model LI-200R, Skye Instruments model SKS 1110) compare favorably to specifications for Moderate and Good Quality classifications (WMO) and for Second Class and First Class classifications (ISO), but their limited spectral sensitivity means they do not meet the spectral selectivity specification necessary for WMO or ISO classification. Silicon-cell pyranometers are generally a third to half the cost of Moderate Quality and Second Class pyranometers. A pyranometer with a thermopile detector and acrylic diffuser is also available (Apogee Instruments model SP-510), with performance characteristics similar to blackbody thermopile pyranometers, but with a cost similar to silicon-cell pyranometers.

Table 1. Specifications for classification of pyranometers according to World Meteorological Organization (WMO) and International Organization for Standardization (ISO).

WMO classification	High quality	Good quality	Moderate quality
ISO classification	Secondary standard	First class	Second class
Specifications			
Response time, s (to 95% of final value)	< 15	< 30	< 60
Zero offset response, W m^{-2} (to 200 W m^{-2} net thermal radiation, ventilated)	7	15	30
Zero offset response, W m^{-2} (to 5 °C h^{-1} change in ambient temperature)	± 2	± 4	± 8
Resolution, W m^{-2} (smallest detectable change)	± 1	± 5	± 10
Stability, % (relative change in sensitivity per year)	± 0.8	± 1.5 (WMO) ± 1.6(ISO)	± 3.0 (WMO) ± 2.0 (ISO)
Nonlinearity, % (relative deviation from sensitivity at 500 W m^{-2} over range of 100 to 1000 W m^{-2})	± 0.5 (WMO) ± 0.2 (ISO)	± 1.0 (WMO) ± 0.5 (ISO)	± 3.0 (WMO) ± 2.0 (ISO)
Directional response, W m^{-2} (absolute deviation from 1000 W m^{-2} direct beam)	± 10	± 20	± 30
Tilt response, % (relative deviation due to tilt from horizontal to vertical at 1000 W m^{-2})	± 0.5	± 2.0	± 5.0
Temperature response, % (relative deviation over an interval of 50 °C)	± 2.0	± 4.0	± 8.0
Spectral selectivity, % (relative deviation of spectral sensitivity from mean spectral sensitivity)	± 2.0	± 5.0	± 10

Shortwave Irradiance Measurement Error Sources

Errors in SW$_i$ measurements can be separated into two groups:

1. Sensor characteristics (calibration, directional, spectral, temperature response, and stability).

2. General use (installation, dirt/dust, and moisture).

Calibration Error

Calibration is accomplished by deriving a calibration factor (CF) that scales the signal output by a thermopile or photodiode detector to match a reference measurement of SW$_i$:

$$CF = \frac{SW_i}{S} \qquad [5]$$

where S is signal output by the pyranometer (typically voltage, but amperage for some models) and CF is in units of W m^{-2} per unit of signal (V or A). Subsequent measurements are then made by rearranging Eq. [5] to solve for SW$_i$ and multiplying the measured S by CF.

The reciprocal of CF is sensitivity and is often reported. Sensitivity provides an indication of the necessary resolution of the analog signal measurement. For example, a typical sensitivity for a blackbody thermopile pyranometer is 10 µV per W m^{-2}. This means the sensor outputs 10 µV for every 1 W m^{-2} of incident shortwave radiation. To yield SW$_i$ measurement resolution of 1 W m^{-2}, a voltage

resolution of 10 μV is required, and 1 μV resolution is required to achieve 0.1 W m^{-2}. This resolution is not available on all meters and dataloggers.

Analysis of the energy balance of a blackbody detector plate indicates multiple radiometer properties contribute to the voltage signal generated by the thermopile (Campbell et al., 1978; Campbell and Diak, 2005; Fairall et al., 1998; Ji and Tsay, 2000). For thermopile pyranometers these include shortwave transmittance of the dome, shortwave absorptance of the blackbody surface, thermal emittance of the blackbody surface, thermal conductivity of the detector plate, and temperature of the sensor body. For silicon-cell pyranometers, contributing factors are shortwave transmittance of the diffuser and shortwave absorptance of the silicon-cell. These factors are accounted for in calibration. Pyranometers should be calibrated in conditions similar to those in which they will be used. Alternatively, for laboratory calibrations, the reference pyranometer should be the same model as the pyranometer being calibrated.

Pyranometer calibrations should be traceable to the World Radiometric Reference (WRR) in Davos, Switzerland. The WRR is an absolute cavity radiometer that is self-calibrated by applying an electric current that duplicates the signal generated by incident solar radiation. Working reference absolute cavity radiometers are periodically calibrated against the WRR. Secondary standard pyranometers can then be calibrated against working reference cavity radiometers and can be used as transfer standards. Transfer standard calibrations are typically done outdoors over the course of a day or multiple days using component summation to measure reference SW$_i$. Component summation refers to independent measurements of the direct and diffuse components of SW$_i$ and summation to yield SW$_i$. Secondary standard pyranometers with calibration traceable to the WRR should be used by pyranometer manufacturers for calibration.

Pyranometer calibration procedures differ among manufacturers, with outdoor and indoor calibration procedures in use. Outdoor calibration typically consists of simultaneous measurement of SW$_i$ from component summation, or from a secondary standard pyranometer, and S from the pyranometer to be calibrated, over the course of a day. The advantage of this approach is characterization of CF with solar zenith angle. A component summation calibration method that accounts for thermal offset of thermopile pyranometers has been proposed (Reda et al., 2005). Often, CF at 45° zenith angle is used, but a zenith angle-dependent CF can be applied to account for changes in CF with zenith angle (Raïch et al., 2007). A short-term shade and unshade method has also been used, which allows for subtraction of the signal when the pyranometer is shaded from signal when the pyranometer is unshaded. This minimizes the influence of thermal offset (for thermopile pyranometers) on calibration because thermal offset should be the same for the shaded and unshaded condition (Philipona, 2002; Reda et al., 2005). This method requires accurate measurement of the direct component of SW$_i$ because the difference between unshaded and shaded signal from the pyranometer is proportional to the direct component of SW$_i$. A shade and unshade method is often used for indoor calibration and requires SW$_i$ measurement with a transfer standard pyranometer and S measurement with the pyranometer to be calibrated. Time is required for the pyranometers to equilibrate when shaded and unshaded, with 20 to 60 time constants being typical equilibration times. If reference SW$_i$ is incorrect during calibration, error will be transferred to the pyranometers being calibrated. Calibration uncertainty is not reported by all manufacturers of

blackbody thermopile pyranometers, but those with published specifications list between 1 and 2%. Calibration uncertainty for silicon-cell pyranometers is often reported as 5%. Temperature should be recorded during calibration, allowing for temperature correction once the pyranometer is deployed in the field.

Pyranometer manufacturers typically recommend recalibration at two-year intervals. Verification of calibration accuracy should be done at least annually, and can be done by comparison to a reference instrument in the same location. Another alternative method is to compare shortwave irradiance measurements to modeled global shortwave irradiance for clear sky conditions (SW_{ic}). Multiple clear sky global shortwave irradiance models are available (Atwater and Ball, 1978; Gueymard, 2008; Lefèvre et al., 2013; Meyers and Dale, 1983). A recent book by Myers (2013) discusses shortwave radiation modeling. A commonly used model in agricultural applications is contained within the net radiation sub-model of the American Society of Civil Engineers (ASCE) standardized reference evapotranspiration equation (ASCE-EWRI, 2005). A user-friendly version of this model is available online at clearskycalculator.com (verified 17 July 2016). On clear days, SW_{ic} can be used as a reference for estimating pyranometer accuracy. Recalibration is recommended if measured SW_i consistently deviates more than 5% from SW_{ic} on clear sky days near solar noon. Blonquist et al. (2010) analyzed model accuracy for clear sky days and reported ± 3% as a reasonable estimate of accuracy for nonpolluted summer days near solar noon. This is consistent with uncertainty estimates for other shortwave irradiance models (Gueymard, 2012). In addition to SW_{ic} being a reference for recalibration requirements, the ratio SW_i/SW_{ic} provides an estimate of cloudiness.

Directional Error

Directional or angular response error results from imperfect cosine correction. Cosine correction means that the sensor is accurate at all incidence angles. Lambert's cosine law states that radiant intensity is directly proportional to the cosine of the angle between the incident radiation beam and a plane perpendicular to the receiving surface. A radiometer that accurately measures radiation according to Lambert's cosine law is said to be cosine corrected. Directional response is often called cosine response and directional error is often called cosine error.
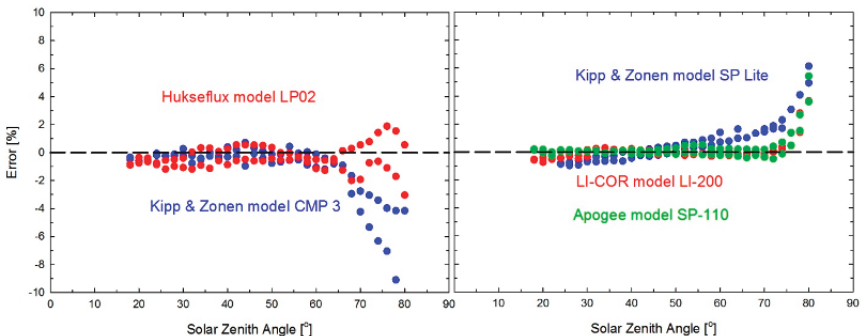
Directional response of blackbody thermopile pyranometers is influenced by multiple radiometer properties, including spatial uniformity of the domes and blackbody absorber, and alignment of domes with respect to the absorber. Similarly, spatial uniformity and alignment of the diffuser with respect to the underlying silicon detector influences directional response in silicon-cell pyranometers. Blackbody and silicon-cell absorbers must be horizontal, the leveling device must be in the same plane as the absorber, and the sensor must be exactly level.

Directional response is often specified as deviation from true cosine response, where a radiation beam of known intensity is used to determine directional response in the laboratory. True cosine response is beam intensity at a zenith angle of zero multiplied by the cosine of the angle between the direct beam and sensor. A common directional response specification for pyranometers is deviation of less than 10 W m^{-2} from a direct beam of 1000 W m^{-2} up to an incidence angle of 80°. The cosine of 80° is 0.174, so irradiance from a 1000 W m^{-2} direct beam is 174 W m^{-2} at 80°. Thus, a pyranometer with this specification should measure within the range 164 to 184 W m^{-2} at a zenith angle of 80°. This specification can

be interpreted in terms of relative error by dividing 10 W m^{-2} by 174 W m^{-2}. Thus, an absolute error of 10 W m^{-2} at an 80° incidence angle is a relative error of 5.7%. If the directional error specification is 20 W m^{-2} up to 80°, then relative error at 80° is double that for 10 W m^{-2} (11.4%). For a directional error specification of 5 W m^{-2}, relative error is half that at 80° (2.9%).

Another method of determining directional response is to compare SW_i measurements on a clear day against reference SW_i (often from component summation, the sum of independent measurements of direct and diffuse SW_i components as explained in the previous section). Reference SW_i must be assumed to represent true SW_i when using field measurements to determine directional response. Directional responses of two common second class blackbody thermopile pyranometers and three common silicon-cell pyranometers indicate errors less than 2% for solar zenith angles between 20° and 60°, and less than 5% for solar zenith angles less than 75° (Fig. 4). We have measured and compared directional response data for multiple replicates of the same pyranometer models at our outdoor calibration facility in Logan, Utah (UT), United States, and found similar results. Reference SW_i was mean SW_i calculated from four secondary standard pyranometers (Hukseflux model SR20, Kipp & Zonen models CMP 11, CM 11, and CM 21) calibrated at National Renewable Energy Laboratory (NREL). Habte et al. (2014) compared multiple thermopile and blackbody pyranometers to reference SW_i and found differences were typically less than 5% for zenith angles less than 60° under clear sky conditions. Differences increased for solar zenith angles greater than 60°.

Directional errors can be significant in applications where hourly (or higher frequency) data are required. Directional errors can also be significant at high latitudes in winter when the sun is low in the sky. A pyranometer with poor directional response may be calibrated to provide accurate measurements in the summer when zenith angles are low for much of the day at mid and high latitude locations, but may have much larger errors during winter months when zenith angles are always high. Over daily time scales, directional errors are reduced by calibrating pyranometers to daily total SW_i. Most of the daily total SW_i is received

Fig. 4. Directional error (cosine error) for two common second class blackbody thermopile pyranometers (Hukseflux model LP02 and Kipp & Zonen model CMP 3) and three common silicon-cell pyranometers (Apogee Instruments model SP-110, Kipp & Zonen model SP Lite, and LI-COR model LI-200). Data were collected during a Broadband Outdoor Radiometer Calibration (BORCAL) at the National Renewable Energy Laboratory (NREL) in Golden, Colorado, United States.
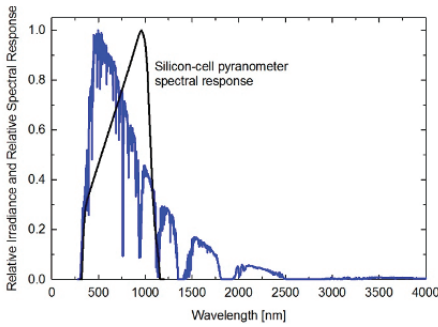
Fig. 5. Relative spectral response of a typical silicon-cell pyranometer (normalized to maximum response at 960 nm) compared to a relative global shortwave irradiance spectrum (normalized to maximum irradiance at 495 nm) at Earth's surface. Silicon-cell pyranometers subsample the shortwave spectrum (350–1100 nm) and thus have spectral errors when the spectrum changes.

in the middle of the day when solar zenith angles are low. Solar zenith angle dependent calibration factors have been used to minimize directional errors (King et al., 1997).

Spectral Error

Spectral error occurs when the detector is not uniformly sensitive to all wavelengths within the shortwave radiation spectrum, or when a dome is not uniformly transmissive to all wavelengths within the shortwave spectrum. Blackbody thermopile pyranometers have minimal spectral error because they are nearly uniformly sensitive to wavelengths from at least 290 to 3000 nm. Spectral sensitivity varies slightly among models due to different materials used to make the domes, as some materials are not uniformly transmissive near the lower and upper bounds of the shortwave spectrum (280 nm and 4000 nm, respectively), but this results in negligible errors. However, silicon-cell pyranometers can have large spectral errors because they subsample the shortwave spectrum (350 to 1100 nm), and are not equally sensitive within this range (Fig. 5). Subsampling and extrapolation are common in scientific measurements for prediction beyond the sample, but extrapolation must always be done with caution. Silicon-cell pyranometers are typically calibrated against blackbody thermopile pyranometers under clear sky conditions, thus they are accurate for clear sky conditions of similar humidity. However, changes in atmospheric air mass, humidity, clouds, dust, or pollution alter the shortwave irradiance spectrum and cause spectral errors.

Atmospheric air mass is the relative mass of the air column between the top of the atmosphere at the solar zenith and a point at Earth's surface. Atmospheric air mass changes as a function of solar zenith angle. At low solar zenith angles near solar noon (low atmospheric air mass), the sky is blue on clear days because Rayleigh scattering is more effective at scattering short wavelength (blue) radiation in the visible spectrum. At high solar zenith angles near the beginning and end of the day (high atmospheric air mass) solar radiation traverses a long atmospheric path before reaching Earth's surface. As a result, the sky looks red because Rayleigh scattering has selectively scattered the shorter wavelength (blue) radiation. Thus, from morning to midday to evening sky color changes from red to blue to red. This alters the signal output of silicon-cell pyranometers because they are more sensitive to red and near infrared radiation than to blue radiation (Fig. 5).

Directional or angular response of silicon-cell pyranometers includes both a directional and spectral component (directional response in the field is the combination of the true directional response as measured in the laboratory and spectral response of the sensor). Spectral error at high solar zenith angles (morning and evening) causes silicon-cell pyranometers to read high and directional error at high solar zenith angles causes most pyranometers (silicon-cell and blackbody

thermopile) to read low. These two errors often cancel each other and yield small directional errors for silicon-cell pyranometers in the field (King and Myers, 1997; Klassen and Bugbee, 2005; Selcuk and Yellott, 1962), except for solar zenith angles greater than about 75° where spectral error dominates (Fig. 4).

Because it is challenging to separate spectral error and directional error, manufacturers of silicon-cell pyranometers optimize diffusers to achieve minimum error as a function of solar zenith angle. This amounts to designing sensors to intentionally read low at high angles of incidence in the laboratory to account for spectral error at high solar zenith angles in the field. Thus, spectral errors due to changes in air mass are largely accounted for in instrument design. Only at high atmospheric air mass (high solar zenith angles) do significant errors occur (Fig. 4, the sharp increase in silicon-cell pyranometer error at solar zenith angles greater than 75° is largely due to spectral error from the increasing proportion of red and near infrared wavelengths within the 350 to 1100 nm range).

Over the relatively narrow range of atmospheric vapor pressure variability, 0.2 to 2 kPa, in Logan, UT, silicon-cell pyranometer errors (relative to the mean of measurements from four secondary standard blackbody thermopile pyranometers) on clear days near solar noon were not statistically significant, and there was no correlation between error and atmospheric vapor pressure over this range. The spectral error may be larger over a wider range of vapor pressure, but it is likely smaller than the error under cloudy conditions (discussed below).

Spectral error can be calculated if sensor spectral sensitivity, spectrum of the radiation source the sensor was calibrated with, and spectrum of radiation source the sensor is measuring are available:

$$\text{Error} = \frac{\int S_\lambda I_{\lambda\text{Measurement}} d\lambda \int I_{\lambda\text{Calibration}} d\lambda}{\int S_\lambda I_{\lambda\text{Calibration}} d\lambda \int I_{\lambda\text{Measurement}} d\lambda} \tag{6}$$

where S_λ is relative (normalized to maximum) pyranometer spectral sensitivity, $I_{\lambda\text{Measurement}}$ is relative (normalized to maximum) spectrum of radiation source being measured, $I_{\lambda\text{Calibration}}$ is relative (normalized to maximum) spectrum of radiation source the pyranometer was calibrated to, and λ is wavelength. As stated, silicon-cell pyranometers are usually calibrated against blackbody thermopile pyranometers under clear sky conditions, thus $I_{\lambda\text{Calibration}}$ is a clear sky spectrum. Silicon-cell pyranometers are therefore most accurate for clear sky conditions with humidity similar to that during calibration.

Spectral response varies slightly among models of silicon-cell pyranometers, due to diffuser materials and variability in silicon-cell options, but S_λ is similar among models because it is largely determined by the spectral properties of silicon. The silicon-cell pyranometer spectral response data from Fig. 5 were input into Eq. [6] to estimate spectral error for silicon-cell pyranometers under cloudy conditions. Using a clear sky calibration spectrum and overcast sky measurement spectrum (both measured during June 2013 in Logan, UT, with an ASD model FieldSpec Pro spectroradiometer) spectral error was predicted to be 9.6% high under overcast conditions. Kerr et al. (1967) studied this error and reported that SW_i on an overcast day was 11.3% of SW_i on a clear day and SW_i weighted according to the spectral response of silicon on the overcast day was 12.6%, which results in a spectral error of 11.5% (ratio of 12.6/11.3) on the overcast day if the
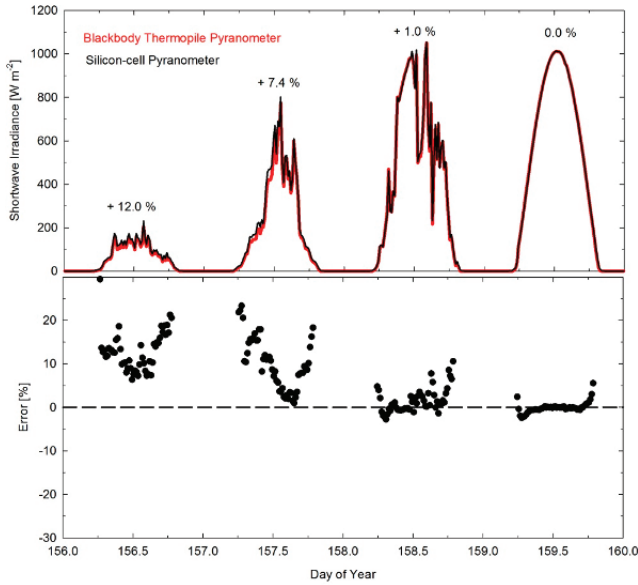
Fig. 6. Spectral error of a silicon-cell pyranometer caused by changes in cloudiness. The reference was a secondary standard blackbody thermopile pyranometer (Kipp & Zonen model CMP 11). This was compared with a silicon-cell pyranometer (Apogee Instruments model SP-110). Over a four-day period, conditions transitioned from overcast to clear sky. Errors for the silicon-cell pyranometer were calculated on daily total basis (daily total error shown in upper graph) and on a fifteen minute interval (lower graph). All silicon-cell pyranometers are subject to this spectral error.

sensor was calibrated on a clear day. This error is similar to the result of 9.6% calculated from Eq. [6] using the spectral data collected in Logan, UT. Shortwave irradiance measurements from silicon-cell pyranometers confirm these predicted errors for cloudy conditions. Measurements were made over a four-day period (5–8 June 2007, in Logan, UT) with a secondary standard thermopile pyranometer (Kipp & Zonen model CM 11) and a silicon-cell pyranometer (Apogee Instruments model SP-110). Spectral error for the thermopile pyranometer should be zero, so it was used to provide reference SW_i. Over the four-day period, conditions transitioned from complete cloud cover to clear sky, with spectral errors (calculated on a daily total basis) for the silicon-cell pyranometer declining from 12.0% under completely overcast conditions to 0.0% for clear sky conditions (Fig. 6). Error of a silicon-cell pyranometer (LI-COR model LI-200) relative to secondary standard thermopile pyranometers (mean of four replicates in the Apogee calibration facility) plotted versus cloudiness (ratio of measured SW_i to modeled clear sky SW_i) indicates errors typically less than 5% until the ratio of actual SW_i to clear sky SW_i (SW_i/SW_{ic}) declines below about 0.3, then errors increase (Fig. 7). Scatter in the error data results from different cloud types, as the magnitude of error will vary with cloud thickness and water content.

It is challenging to determine spectral error for silicon-cell pyranometers when sky conditions are dusty or polluted because solar radiation spectra or simultaneous data from a blackbody thermopile and silicon-cell pyranometers during dusty and polluted conditions are required. Throughout August 2015, Logan, UT,
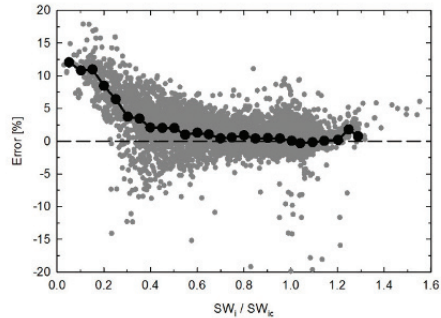
experienced a high level of atmospheric smoke from wildfires in the Pacific Northwest. Comparison of silicon-cell pyranometers to mean SW_i from four secondary standard blackbody thermopile pyranometers on a smoky day (visibility reduced to 6 km and PM 2.5 of 100 mg m^{-3}) and a clear day (visibility of 30 km and PM 2.5 of 5 mg m^{-3}) revealed differences of less than 2%. It is possible aerosols or dust will have a different effect.

Fig. 7. Spectral error of a silicon-cell pyranometer as a function of cloudiness (SW_i/SW_{ic}, ratio of measured SW_i to modeled clear sky SW_i, often called the cloudiness index and serves as a surrogate variable for cloudiness). Error for the silicon-cell pyranometer (LI-COR model LI-200) was calculated relative to the mean of four secondary standard blackbody pyranometers. Black line is a bin average. All silicon-cell pyranometers will have this spectral error and follow a similar pattern with cloudiness. The magnitude of error varies with cloud thickness and water content, resulting in the scatter around the average error.

Temperature Error

Temperature error results from the temperature sensitivity of sensor components (thermopile or silicon-cell detector, resistor). Temperature sensitivity specifications are typically lower for blackbody thermopile pyranometers, particularly first class and secondary standard pyranometers, than for silicon-cell pyranometers. Most blackbody thermopile pyranometers are specified at less than 4% sensitivity from -10 to 40 °C (0.08% per °C, assuming temperature response is linear). Silicon-cell pyranometers are often specified at less than 0.15% per °C, about twice the sensitivity of many blackbody thermopile pyranometers. Secondary standard blackbody thermopiles are specified at 1.0% variability or lower for a temperature range of at least -10 to 40 °C. Some blackbody thermopile pyranometer manufacturers offer models with a temperature sensor and characterized response (e.g., EKO model MS-80, Hukseflux model SR20, or Kipp & Zonen model CMP 21), so users can correct for the temperature effect.

Blackbody thermopile pyranometers can also have thermal offset errors associated with net longwave radiation and rapid heating and/or cooling. If the dome and sensor body (housing) temperatures are different, this influences the energy balance of the detector plate and can cause measurement error. The longwave radiation balance at the blackbody surface is zero when the surface and glass dome are at the same temperature, but rapid heating or cooling and negative net longwave radiation (caused by exposure to the cold sky) result in signal gain or loss due to longwave energy transfer. Some models of blackbody thermopile pyranometers have ventilation units attached to them to minimize temperature differences between components.

There are two types of thermal offset errors: Zero Offset A and Zero Offset B. Both offsets are determined in the dark. Zero Offset A is response to thermal radiation of 200 W m^{-2} and Zero Offset B is the response to a temperature change of 5 °C per hour. Specifications for Zero Offset A range from 10 to 15 W m^{-2} for second class pyranometers to 3 to 6 W m^{-2} for secondary standard pyranometers. Specifications for Zero Offset B range from 4 to 6 W m^{-2} for second class pyranometers to

1 to 2 W m^{-2} for secondary standard pyranometers. Double domed sensors have lower offsets than single domed sensors because of the additional insulative layer of air.

Zero Offset A is dependent on the longwave radiation balance between the sky and dome. It is negative because the dome emits more longwave radiation than it is absorbing from the sky (dome is warmer than the sky), reducing its temperature relative to the blackbody absorber. Thus, the blackbody absorber emits more longwave radiation to the dome than it receives from the dome. Magnitude of this thermal offset is greatest during the day due to solar heating of the sensor (Ji and Tsay, 2010; Philipona, 2002), especially under clear sky and calm conditions, but it is also present at night (small negative signals are measured at night). Much lower offsets occur on cloudy days (Haeffelin et al., 2001). Subtraction of the nighttime signal has been used to partly correct for daytime heat loss due to radiative cooling (Dutton et al., 2001). Calibration of pyranometers should include correction for the thermal offset (Reda et al., 2005). Errors due to daytime radiative cooling can be corrected with measurements of net longwave irradiance (from a pyrgeometer) and ambient air temperature.

Thermal offsets are reduced by ventilation, which reduces temperature differences between components (dome and detector). Ventilation units that provide air flow over the outer dome are commonly available (e.g., EKO Instruments model MV-01, Eppley Laboratory model VEN, Hukseflux model VU01, Kipp & Zonen model CVF4), but they require 5 to 10 W of power. Internal ventilation, air flow between the inner and outer domes (e.g., Hukseflux model SR30), reduces thermal offset more than external ventilation and typically uses less power. Another method of reducing thermal offset is the use of a sapphire dome (e.g., Hukseflux model SR25), which has a much higher thermal conductivity than quartz and better matches the thermal conductivity of the sensor body, thus reducing the temperature difference between dome and detector. A design with a quartz diffuser over the blackbody detector and a single glass dome over the diffuser (e.g., EKO Instruments model MS-80) has also been used to reduce thermal offset by improved thermal coupling of the detector, diffuser, and dome, reducing the temperature difference.

Silicon-cell pyranometers operate via the photoelectric effect and are not subject to these thermal errors. Thus, they do not have specifications for Zero Offset A and Zero Offset B. They have been reported to have a negative temperature response (Klassen and Bugbee, 2005). This is based on the response of open circuit voltage of silicon-cells (solar panels operate in open circuit mode), which declines with increasing temperature (Osterwald, 1986). However, silicon-cell pyranometers operate in short circuit mode. This means that the temperature sensitivity of a silicon-cell is wavelength dependent, with a negative response below about 500 nm and a positive response above about 900 nm (Fig. 8). This makes temperature sensitivity dependent on the spectral intensity of the radiation source being measured. For sunlight, spectral intensity is greatest near 500 nm (Fig. 5), in the range where silicon-cell temperature response is slightly negative. Silicon-cell sensitivity peaks at about 960 nm (Fig. 5), where the temperature coefficient is positive. Sunlight includes radiation at all wavelengths across the silicon sensitivity range (350–1100 nm), making the temperature response of silicon-cell pyranometers for sunlight complex and dependent on the solar spectrum, silicon-cell sensitivity, and wavelength-dependent temperature coefficient.
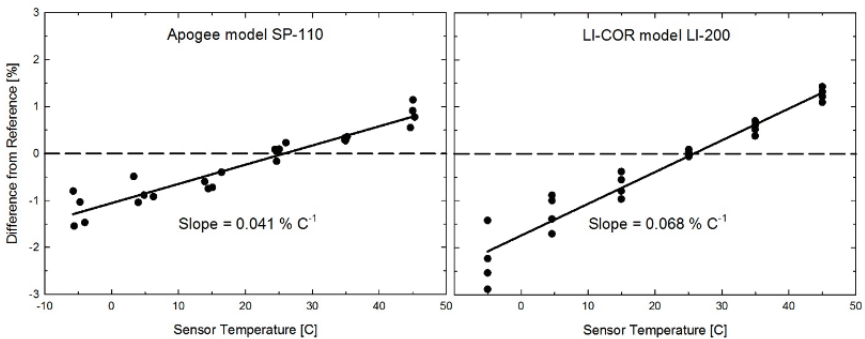
To determine the temperature response silicon-cell pyranometers, four repli-cates of each of two models (Apogee Instruments model SP-110 and LI-COR model LI-200) were placed in a freezer and allowed to equilibrate. The sensors were then removed and immediately placed outside under clear sky conditions near solar noon. Sensor output was continuously monitored as they warmed over thirty min-utes. Measurements were compared to shortwave radiation measurements from a reference blackbody thermopile pyranometer (Hukseflux model SR11) and plotted versus the silicon-cell pyranometer temperature (Fig. 9). Silicon-cell pyranometer temperature was continuously measured with thermistors mounted inside the four SP-110 pyranometers. The LI-200 pyranometers were assumed to be equal to the mean temperature from the SP-110 pyranometers. Results indicate a positive, linear temperature coefficient (Fig. 9) of 0.04 to 0.07% per °C under sunlight. These tem-perature coefficients are slightly lower than a previously reported value of 0.082% per °C for LI-COR model LI-200 pyranometers (King and Myers, 1997) and within the 0.04 to 0.10% per °C range reported by Kerr et al. (1967) for silicon-cells. The temperature response is challenging to measure accurately. One anomalous study found a much larger, nonlinear temperature response of LI-200 pyranometers, with a decline of about 5% from 25 °C to 10 °C (Raïch et al., 2007).

Blackbody thermopile and sil-icon-cell pyranometer temperature responses are usually considered negligible for most applications, as they are typically much smaller than other sources of error. For example, if the temperature coefficient was 0.05% per °C and daytime temper-ature variability was 20 °C (36 °F), then signal change due to temper-ature would be 1%. Temperature correction may be more applicable on a seasonal time scale, where tem-perature changes can be much larger than 20 °C. Temperature sensitivity
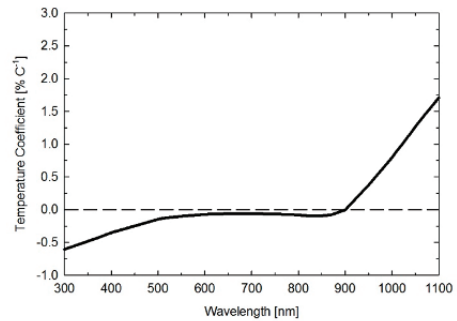
Fig. 8. Wavelength-dependent temperature coefficient of a typical silicon-cell in short-circuit mode.

Fig. 9. The temperature response of two silicon-cell pyranometers (Apogee Instruments model SP-110 and LI-COR model LI-200). The slope is the mean temperature response of four replicate sensors.

of silicon-cell pyranometers is linear (Fig. 9), so the signal can be corrected for temperature changes if a measurement or estimate of detector temperature is available. All silicon-cell pyranometers are likely to have positive temperature coefficients with a similar slope when measuring sunlight because the measured data match the expected temperature sensitivity based on the wavelength-dependent temperature coefficient (Fig. 8). These results will be different if the radiation source is not the sun. As an example, the temperature response of ten replicate silicon-cell pyranometers (Apogee Instruments model SP-110) was determined in a temperature-controlled chamber under a cool white light emitting diode (LED) lamp with a high fraction of blue radiation below 500 nm and negligible output at wavelengths greater than 800 nm. As expected, based on the wavelength-dependent temperature sensitivity of silicon-cells (Fig. 8), the temperature coefficient was negative (-0.043% per °C).

Stability

Long-term stability of pyranometers is dependent on optical stability (glass dome and blackbody absorber surface for blackbody thermopile pyranometers, and acrylic diffuser for silicon-cell pyranometers) and electrical stability (thermopile or silicon-cell detectors, resistors, and solder joints). Some blackbody thermopile pyranometers are sensitive to the stability of the blackbody surface, which is subject to fading and discoloration with exposure to shortwave radiation. In a recent publication, Wood et al. (2015) measured the drift in two replicate Eppley model PSP pyranometers. Discoloration (greening) of the blackbody surface on PSP pyranometers caused downward drift in signal, leading to low measurements of SW_i. An initial stable period was observed, which varied among replicates. Similar rates of downward drift, approximately -1.5% per yr, were measured once drift started to occur. Downward drift of Eppley PSP pyranometers was also reported in an earlier study, but at lower rates of -0.4 to -1.0% per yr (Riihimaki and Vignola, 2008). Downward drift of Eppley PSP pyranometers was found to be a linear function of exposure to shortwave radiation, thus cumulative exposure can be used to predict signal decline as a result of fading or discoloration of the blackbody detector.

In addition to documenting drift in Eppley PSP pyranometers, Wood et al. (2015) proposed a method that uses time series of three different ratios (SW_i to extraterrestrial shortwave irradiance, PAR to SW_i and PAR to extraterrestrial shortwave irradiance) to detect drift in pyranometers. Using the proposed method and time series of radiation ratios, Wood et al. (2015) measured downward drift in multiple Eppley PSP pyranometers and upward drift in two Kipp and Zonen CM 3 pyranometers at field research sites in a measurement network. Drift of PSP pyranometers was consistent with fading of the blackbody detector. The exact cause of upward drift in CM 3 pyranometers was not determined, but was possibly attributed to increased electrical resistance. As discussed above, comparison with modeled SW_i for clear sky conditions can provide a reasonable estimate of drift and need for recalibration.

We have four secondary standard pyranometers (Hukseflux model SR20, Kipp & Zonen models CMP 11, CM 11, and CM 21) in our calibration facility at Apogee Instruments in Logan, UT. Each pyranometer is sent to NREL every two to three years for recalibration. The oldest one is the CM 21 (purchased in 2004), and this instrument had a large decline of 1.8% between June 2008 and

May 2011. Two calibrations since May 2011 (June 2013 and June 2015) indicate that the pyranometer is stable. After June 2008, NREL started using an updated method to account for pyranometer thermal offset (Reda et al., 2005). This particular CM 21 has a large thermal offset compared with the other three secondary standard pyranometers. It is likely that use of the new calibration method caused apparent drift, rather than actual change in calibration, as the new calibration method better accounted for the thermal offset. The other three secondary standard pyranometers have been stable at less than 1% change between calibrations. Visual analysis indicates no discoloration of the blackbody detectors on any of these four pyranometers. Multiple replicates of three models of silicon-cell pyranometers (Kipp & Zonen model SP-Lite, LI-COR model LI-200, and Apogee Instruments model SP-110) were compared to the mean of these four secondary standard pyranometers over a two-year period (August 2013–August 2015). Data for clear sky conditions indicate none of the silicon-cell pyranometers has drifted by more than 2% per yr. Only one of the sensors drifted by more than 1% per yr, an SP-Lite drifted down by -1.2% per yr. Tanner (2001) found that the change in calibration for 520 LI-200 pyranometers was less than 2% per yr for 86% of sensors, and only 6% of pyranometers drifted by more than 3% per yr. Geuder et al. (2014) reported change in calibration for 30 LI-200 pyranometers, with only one drifting by more than 2% per year.

Drift problems can be temporarily corrected by recalibration, but regular recalibration is required to account for continued drift. It should be noted that recalibration only partially fixes the problem in the case of physical changes in sensor optics (e.g., discoloration of blackbody surface). Wood et al. (2015) reported that discoloration of blackbody detector surfaces resulted in changes in spectral response, meaning pyranometers with discolored blackbody surfaces were no longer equally sensitive to all wavelengths within the shortwave spectrum. This condition results in spectral errors when measurements are made in conditions significantly different than conditions during calibration. However, to our knowledge, the spectral absorptivity of a discolored blackbody surface has not been published, so the magnitude of spectral error can't be quantified using Eq. [6].

General Use

The most common field errors are improper mounting, inaccurate leveling, and occlusion of the dome or diffuser. Pyranometers should be mounted in an open area away from buildings, trees, and other structures that may obstruct the field of view. On a weather station, pyranometers should be mounted on the south side of the tower in the northern hemisphere and north side of the tower in the southern hemisphere. Other sensors should not obstruct the field of view.

Inaccurate leveling can result from improper installation, drift in mounting hardware following installation, or a level bubble that is not in the exact same plane as the detector. Leveling errors can potentially be detected by comparing measured SW_i to modeled clear sky SW_i (Menyhart et al., 2015).

Occlusion is typically caused by residual precipitation, condensation, or dust and/or debris deposition caused by wind or birds. Dust occlusion can be particularly bad when the dome or diffuser is wet, following dew deposition or precipitation. Glass domes on blackbody thermopile pyranometers and diffusers on some models of silicon-cell pyranometers are dome-shaped, and can be self-cleaning. Periodic cleaning is recommended, and frequency of cleaning

is dependent on local conditions. Some pyranometer models include a heater and/or ventilation unit to minimize errors due to dew, frost, rain, and snow. Power requirements for heated and/or ventilated pyranometers vary over a 100-fold range, from 0.2 to 20 W. Power consumption increases with size of the pyranometer, number of resistance heaters, and size of the fan. For units with a heater and ventilator, approximately half the power goes to heating and the other half to ventilation. Ventilator filters should be cleaned or replaced at least annually to maintain proper air flow. The necessary interval varies widely depending on moisture and dust in the air.

Measurement Uncertainty

Collectively, the sources of error described above contribute to significant uncertainty in SW_i measurements. A recent report indicated measurement uncertainty of about 4% and 8% for SW_i measurements with blackbody thermopile and silicon-cell pyranometers, respectively (Reda, 2011). The uncertainty calculation method proposed by Reda (2011) was based on the International Guidelines of Uncertainty in Measurement (JCGM/WG 1, 2008). The main contributor to the 4% greater uncertainty estimate for silicon-cell pyranometers is their limited spectral response. Aside from this, calibration uncertainty was the largest contributor to total measurement uncertainty for both types of pyranometers, and was estimated at nearly one third of total uncertainty. When solar zenith angle–dependent calibration factors were used, rather than constant calibrations factors, total measurement uncertainty was reduced by about half. The uncertainty estimates of Reda (2011) are similar to those reported by Klassen and Bugbee (2005), 2 to 3% for thermopile pyranometers and 3 to 6% for silicon-cell pyranometers. These estimates provide an approximation of uncertainty in SW_i measurements with pyranometers.

Direct and Diffuse Shortwave Irradiance

This section, Shortwave Irradiance, has discussed global horizontal shortwave irradiance (SW_i) measurements with pyranometers. As discussed in the Theory section, SW_i is the sum of direct and diffuse components. The direct component is determined by measuring direct normal irradiance (DNI, irradiance on a plane perpendicular to sun) with a pyrheliometer and multiplying by the cosine of the solar zenith angle. The diffuse component is called diffuse horizontal irradiance (DHI, radiation emanating from entire hemisphere of sky when the solar disk is blocked from the field of view) and is measured with a pyranometer shaded by a solar tracking disk. Summation of DNI and DHI is referred to as the component summation method for determination of SW_i and has been reported as more accurate than SW_i measurement with pyranometers (Michalsky et al., 1999). However, measurements of DNI and DHI with pyrheliometers and shaded pyranometers, respectively, are complex, expensive, and not common on agricultural weather stations or in agricultural measurement networks. Vignola et al. (2012) discussed DNI measurements with pyrheliometers and DHI measurements with shaded pyranometers in detail.
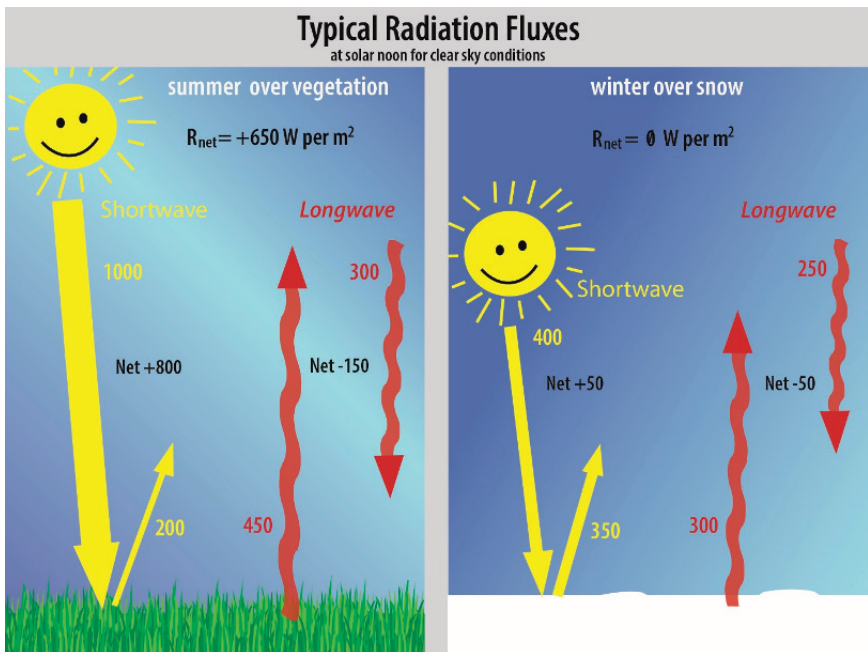
Net Radiation

Net radiation (R_n) at Earth's surface is defined as the difference between incoming (downwelling) and outgoing (upwelling) irradiance, and consists of shortwave and longwave components:

$$R_n = (SW_i - SW_o) + (LW_i - LW_o) \tag{7}$$

where SW_i is incoming (downwelling) shortwave irradiance (global shortwave), SW_o is outgoing (upwelling) shortwave irradiance (reflected shortwave), LW_i is incoming (downwelling) longwave irradiance (global longwave), LW_o is outgoing (upwelling) longwave irradiance (emitted longwave), $SW_i - SW_o$ is net shortwave irradiance (SW_n), $LW_i - LW_o$ is net longwave irradiance (LW_n), and all terms are expressed as energy flux densities (typically in units of W m^{-2}). While net radiation is the name universally used to describe net irradiance at Earth's surface, it should be recognized that all terms in Eq. [7] are irradiance and R_n could be referred to as net irradiance. Typical values of the four components of R_n for clear sky conditions near solar noon in mid-summer and mid-winter provide approximations for magnitudes of expected irradiances (Fig. 10).

Net radiation is a major component of the surface energy balance:

$$R_n - G = H + LE + A_n + S \tag{8}$$

Fig. 10. Typical values of the four components (incoming shortwave irradiance SW$_i$, outgoing shortwave irradiance SW$_o$, incoming longwave irradiance LW$_i$, and outgoing longwave irradiance LW$_o$) of net radiation (R_n) for clear sky conditions near solar noon in mid-summer and mid-winter.

Table 2. Albedo (α, broadband shortwave reflectivity, SW_o/SW_i) of some representative terrestrial surfaces (Campbell and Norman, 1998).

Surface	Albedo (α)
Grass field	0.24–0.26
Wheat field	0.16–0.26
Corn field	0.18–0.22
Deciduous forest	0.10–0.20
Coniferous forest	0.05–0.15
Tundra	0.15–0.20
Steppe	0.20
Fresh snow	0.75–0.95
Old Snow	0.40–0.70
Wet, dark soil	0.08
Dry, dark soil	0.13
Wet, light soil	0.10
Dry, light soil	0.18
Dry, white sand	0.35
Urban area (average)	0.15

where G is ground heat flux, H is sensible heat flux, LE is latent heat flux, A_n is net photosynthesis, S is heat storage (typically negligible in crop canopies, but must be accounted for in forest canopies), and like R_n, all terms are flux densities (typically W m^{-2}). The difference between R_n and G ($R_n - G$) is defined as available energy and is the energy at the surface available to drive surface processes (e.g., heating, evapotranspiration).

In many cases, R_n is the largest term in Eq. [8], thus accurate R_n measurements or estimates are essential to surface energy balance studies. Surface energy imbalance (meaning, measurement of $R_n - G$ is not balanced by the sum of measurements of terms on the right-hand side of Eq. [8]) has received considerable attention (e.g., Foken, 2008; Leuning et al., 2012; Wilson, 2002). Some studies have found R_n measurements have lower uncertainty than turbulent flux measurements (H and LE) in surface energy balance experiments (Twine et al., 2000), while other studies have suggested energy balance studies are limited by R_n accuracy and there is a need for improved net radiometer designs and calibration procedures (Kustas et al., 1998).
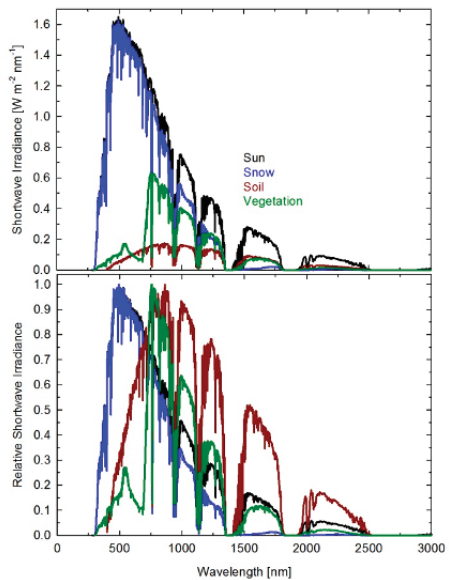
Shortwave Irradiance

Measurement of SW_i was discussed in the previous chapter section, Global Shortwave Irradiance. Measurement of SW_o requires inversion of a pyranometer to measure shortwave irradiance reflected from the ground surface. The same considerations for measurement of SW_i apply to measurement of SW_o. Some additional specifics for SW_o measurement should also be considered. Downward-looking pyranometers should be equipped with a shade ring and mounted so as to eliminate any shortwave radiation not reflected by the surface from reaching the detector (the downward-looking pyranometer shouldn't 'see' above the horizon). Nearly all terrestrial surfaces are diffuse reflectors, meaning reflected radiation is reflected

in all directions, and are relatively isotropic (not directionally dependent), even if radiation from the source illuminating the surface (sun) is directionally dependent (a clear day). As a result, directional response of pyranometers used to measure SW_o is less critical than directional response of pyranometers used to measure SW_i. As long as the distribution of angles of reflected shortwave radiation is relatively constant for diverse surface conditions (plant canopy, soil, or snow), sensors with fairly poor directional response can still yield accurate SW_o measurements if they are calibrated over a diffuse reflecting surface.

The ratio SW_o/SW_i quantifies broadband surface shortwave reflectivity and is called albedo. Albedo of terrestrial surfaces varies over a wide range (Table 2). Albedo also changes with sky conditions. On a clear day albedo is highest when the sun is near the horizon and lowest near solar noon. On an overcast day albedo is nearly constant, assuming the underlying surface doesn't change over the course of the day. The combination of an upward-looking pyranometer and downward-looking pyranometer (typically of the same model), a net shortwave radiometer, is often called an albedometer. A single pyranometer mounted on a rotating device can also be used as a net shortwave radiometer. When measuring SW_n or albedo with this type of device, the pyranometer must be returned to a level position each time the mechanism is rotated to measure SW_i. Also, sky conditions (degree of cloudiness) must be constant for short-term measurements because SW_i and SW_o will not be measured at the same time.

Silicon-cell pyranometers should not be used for SW_o measurement. The spectrum of reflected radiation from terrestrial surfaces is different than the spectrum of incoming radiation (Fig. 11), and the limited and uneven spectral sensitivity of silicon-cell pyranometers (Fig. 5) will be subject to large errors (Table 3). Ross and Sulev (2000) reported errors of 20 to 40% for measurements of SW_o and measurements of shortwave irradiance transmitted below plant canopies with silicon-cell pyranometers. While it is possible to calibrate a silicon-cell pyranometer for specific surface conditions, over the course of a year an agricultural field may change from bare soil, to partial canopy cover, to full green canopy cover, to stubble (following harvest)

Fig. 11. Reflected shortwave irradiance spectra for snow, soil, and vegetation compared to an incoming shortwave irradiance spectrum (absolute values of irradiance are shown in top graph, relative values of irradiance are shown in bottom graph and were calculated by normalizing to the maximum value). Reflectance data were taken from the Advanced Spaceborne Thermal Emission and Reflection (ASTER) spectral library (Baldridge et al., 2009). If a silicon-cell pyranometer is used to measure reflected shortwave irradiance (SW_o) these differences in spectral reflectance cause errors in the measurement (Table 3).
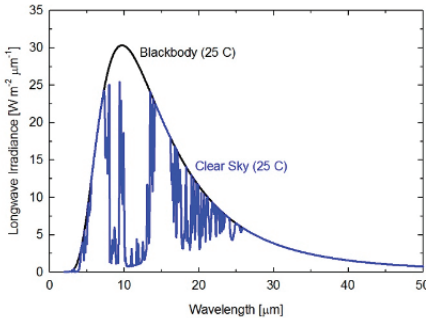
Table 3. Spectral errors in measurement of reflected shortwave irradiance (SW$_o$) with silicon-cell pyranometers calibrated to clear sky conditions. Equation [6] was used to calculate errors.

Surface	Error
	%
Grass canopy	14.6
Deciduous canopy	16.0
Conifer canopy	19.2
Agricultural soil	-12.1
Forest soil	-4.1
Desert soil	3.0
Water	6.6
Ice	0.3
Snow	13.7

or senesced canopy, to bare soil, to snow. Each of these surfaces has a characteristic reflected shortwave irradiance spectrum. A blackbody thermopile pyranometer, with equal sensitivity to all shortwave wavelengths, eliminates spectral error in SW$_o$ measurements under all conditions.

Longwave Irradiance

Longwave irradiance is measured with pyrgeometers (e.g., EKO Instruments model MS-202, Eppley Laboratory model PIR, Hukseflux model IR20, or Kipp & Zonen model CGR 4), which are broadband radiometers similar to blackbody thermopile pyranometers, but fitted with a silicon dome or flat window (instead of a quartz or glass dome) and an interference filter to block shortwave radiation at wavelengths less than about 4.5 μm. Silicon transmits infrared wavelengths and has cutoff between 40 and 50 μm. Thus, the combination of shortwave blocking filter and silicon window and/or dome span most of the range of infrared wavelengths emitted by Earth's surface and Earth's atmosphere (Fig. 12). Longwave radiation spectra for terrestrial surfaces (soil, plant canopy, or snow) are similar to blackbody spectra calculated with Eq. [1], as emissivities for terrestrial surfaces are often near one. However, under clear sky conditions atmospheric longwave radiation spectra are different because air molecules are selective absorbers and emitters, meaning sky absorptivity and emissivity are variable and much less than one at certain wavelengths. Thus, when the sky is clear it appears colder than the surface. Longwave radiation spectra for clear and cloudy sky conditions are also

Fig. 12. Clear sky longwave irradiance for a mid-latitude atmosphere at 25 ˚C compared to blackbody irradiance at 25 ˚C. Many terrestrial surfaces (soil, plant canopy, snow) are nearly blackbody radiators (emissivities are near one), but a clear sky is unique because of selective absorption and emission by atmospheric gases. An overcast sky approximates a blackbody emitter and irradiance is similar to that shown for the blackbody.

different, as the water vapor in clouds makes them nearly blackbody emitters like terrestrial surfaces. As a result, longwave irradiance spectra for overcast conditions can be approximated with Eq. [1] using the effective temperature of the bottom of the clouds. A typical value of incoming global longwave irradiance (LW_i) for a mid-latitude location in summer on a clear day near solar noon is 300 W m^{-2}. A typical value for a cloudy summer day is 400 W m^{-2}. Typical values of outgoing longwave irradiance (LW_o) can be calculated from surface temperature with Eq. [3].

The instrument properties contributing to the energy balance of the absorbing surface of the detector plate in a pyrgeometer are longwave reflectance and transmittance of the dome or window (hereafter referred to as a dome, even though many instruments have flat windows), thermal conductance of the detector plate, and sensor body temperature. These factors are accounted for during calibration, but conditions dissimilar to conditions during calibration can cause measurement errors if there are imperfections in instruments properties (e.g., longwave transmittance of the dome is less than 100%). Pyrgeometer calibration is accomplished by deriving a calibration factor (CF) that scales the signal output by the thermopile to match a measurement of the longwave radiation balance at the detector surface ($LW_{in} - LW_{out}$):

$$CF = \frac{LW_{in} - LW_{out}}{S} \qquad [9]$$

where LW_{in} is incoming longwave irradiance (W m^{-2}) absorbed by the blackbody surface, LW_{out} is outgoing longwave irradiance (W m^{-2}) emitted by the blackbody surface, S is voltage signal output by the thermopile, and CF is in units of W m^{-2} per μV. The reciprocal of CF is pyrgeometer sensitivity. Typical sensitivity for a pyrgeometer is 10 μV per W m^{-2}, meaning signal output is 10 μV for every 1 W m^{-2} difference between LW_{in} and LW_{out}. Resolution of the analog signal measurement must be 10 μV to provide LW_{in} measurement resolution of 1 W m^{-2} and 1 μV to provide 0.1 W m^{-2}.

In Eq. [9] $LW_{out} = \sigma T_D^4$, where T_D is detector temperature in units of K, and is measured with an internal temperature sensor (thermistor or platinum resistance thermometer). The internal temperature sensor should be thermally coupled to the detector plate to provide an accurate estimate of detector temperature. The detector plate and internal temperature sensor should be thermally isolated from the sensor housing adjacent to the plate to minimize the influence of heat transport by conduction. Once a pyrgeometer is calibrated, subsequent measurements of LW_i or LW_o are made by rearranging Eq. [9] to solve for LW_{in} and inputting CF, measured detector temperature, and measured S. Signal from a pyrgeometer directed toward the sky to measure LW_i is typically negative because LW_{in} is typically less than LW_{out}. Signal is often near zero for a pyrgeometer directed toward the ground to measure LW_o because LW_{in} and LW_{out} are similar in magnitude.

Similar to blackbody thermopile pyranometers, error is introduced in measurements of longwave irradiance if the pyrgeometer dome and reference junction temperature are different. This error can be accounted for if a measurement of dome temperature (T_{Dome}) is available:

$$LW_{in} = CF \cdot S + \sigma T_D^4 - k\sigma \left(T_{Dome}^4 - T_{Detector}^4 \right) \qquad [10]$$

where k is factor related to the thermal coupling between dome and detector and must be determined during calibration. Some pyrgeometer models (e.g., Eppley Laboratory model PIR) have a second temperature sensor to provide a measurement of T_{Dome}. Good thermal coupling between dome and detector minimizes k and makes the term on the right-hand side of Eq. [10] negligible. It is also possible to shade pyrgeometer domes to minimize the temperature difference between dome and detector. Shading also reduces transmission of shortwave wavelengths if the shortwave blocking filter is imperfect.

Theoretically, pyrgeometers should equally weight all wavelengths of radiation between approximately 4.5 and 50 μm. In practice, pyrgeometers are not uniformly sensitive to wavelengths within this range because of absorption bands of silicon. This must be accounted for in the calibration procedure, meaning the longwave transmittance of the silicon dome must be accounted for when deriving CF (Eq. [9]). There are two methods for calibrating pyrgeometers: calibration against a reference pyrgeometer under outdoor conditions, or calibration against a blackbody radiation source in the laboratory. Outdoor calibrations should be conducted at night to avoid the influence of solar heating of the silicon dome (Gröbner and Los, 2007). Data from clear and cloudy nights should be included to provide a range of conditions. For laboratory calibration, temperature of a blackbody can be controlled to produce longwave irradiances characteristic of outdoor conditions, and temperature measurement of the blackbody surface can be used to determine emitted longwave irradiance. Pyrgeometer body temperature and blackbody source temperature should be varied to span the range of the conditions expected at the site where the pyrgeometer will be used (Philipona et al., 1995). For pyrgeometers intended to measure LW_i, Philipona et al. (1998) suggested that blackbody calibration source temperature should be 10 to 25 °C below pyrgeometer body temperature. Gröbner and Los (2007) proposed a laboratory calibration method that weights radiation from a blackbody source according to the spectral response of the pyrgeometer to be calibrated. They reported that differences between this method and direct comparison to the World Infrared Standard Group (WISG) under outdoor conditions were less than 1%. The drawback of this method is that the spectral response of the pyrgeometer to be calibrated must be known. Another approach for laboratory calibration is use of a reference pyrgeometer to measure longwave irradiance from the blackbody source and serve as a transfer standard. The reference pyrgeometer should be identical to the pyrgeometer to be calibrated, and it should be calibrated against reference pyrgeometers outdoors. This method assumes that variability in silicon domes is negligible among replicate pyrgeometers of the same model.

Multiple studies have pointed out the lack of a world standard for broadband longwave irradiance measurement that is analogous to the World Radiation Reference for broadband shortwave irradiance (Blonquist et al., 2009a; Brotzge and Duchon, 2000; Halldin and Lindroth, 1992; Ohmura et al., 1998). Progress toward a longwave irradiance standard has been made through the establishment of an interim World Infrared Standard Group (WISG), consisting of four pyrgeometers calibrated against an absolute sky-scanning radiometer (Marty et al., 2003; Philipona et al., 2001). Outdoor calibration to reference pyrgeometers traceable to the WISG has been reported as the current best practice for pyrgeometer calibration (Vignola et al., 2012).

Longwave irradiance is diffuse, whether the radiation source is the sky or Earth's surface. Land surface temperature differences are relatively small for a uniform surface (e.g., full cover crop canopy). Even for nonuniform land surfaces, elements at the surface are often within a few degrees of each other. For clear skies, however, there are temperature and aerosol gradients across the hemisphere of sky (Unsworth and Monteith, 1975). For example, sky temperature for clear conditions is coldest in a direction perpendicular to the surface and gets warmer toward the horizons. Also, partly cloudy skies can produce temperature differences across the hemisphere of sky because clouds are much closer to blackbodies than clear sky. Despite nonuniform sky conditions, angular distribution of longwave radiation has been reported to be similar for clear and overcast skies (Unsworth and Monteith, 1975). Thus, outdoor calibration of pyrgeometers accounts for imperfect directional response. It has also been reported that the distribution of angles of longwave radiation emitted by the atmosphere and a blackbody cavity are similar (Gröbner and Los, 2007), accounting for imperfect directional response of a pyrgeometer if it is calibrated with a blackbody source in the laboratory. Thus, directional response of pyrgeometers is less critical than directional response for upward-looking pyranometers.

Errors from a pyrgeometer with imperfect directional response are typically small compared to the potentially large sources of error due to solar heating of the dome, imperfect spectral sensitivity, and imperfect shortwave radiation blocking. A pyrgeometer with imperfect shortwave radiation blocking due to a filter that is partially transparent to some solar wavelengths will yield high LW_i or LW_o measurements because some fraction of shortwave radiation is transmitted to the blackbody absorber and perceived as longwave radiation.

Solar heating of the dome causes it to be warmer than the underlying blackbody absorber, resulting in increased radiation toward the blackbody surface and errors in LW_i measurement. This has been well documented for Eppley model PIR pyrgeometers with an older KRS-5 dome (Albrecht and Cox, 1977; Enz et al., 1975) and newer versions with a silicon dome (Alados-Arboledas et al., 1988; Perez and Alados-Arboledas, 1999; Udo, 2000). This can result in large LW_i measurement errors on clear and intermittently cloudy days, especially if there is little wind (natural ventilation). Solar heating of the dome can be reduced by shading the dome (Alados-Arboledas et al., 1988; Enz et al., 1975) and/or ventilating the dome (Enz et al., 1975; Perez and Alados-Arboledas, 1999). Corrections for the solar heating effect have also been developed (Alados-Arboledas et al., 1988; Oliveira et al., 2006). Solar heating of the dome should be minimized in pyrgeometer construction by maximizing thermal coupling between the dome and detector plate. A recent study found LW_i measurements from an unshaded Kipp & Zonen model CGR 4 pyrgeometer matched LW_i measurements from a shaded Eppley PIR within the range of measurement uncertainty, indicating that the design of the CGR 4 reduces the solar heating effect (Meloni et al., 2012). Some pyrgeometer manufacturers offer shading devices (e.g., Kipp & Zonen model CM 121B/C, EKO Instruments model RSR-01).

Nonuniform spectral response has been shown to cause errors of about 2% for the range of integrated water vapor content of the atmosphere (Gröbner and Los, 2007; Miskolczi and Guzzi, 1993). Spectral errors for pyrgeometers can be calculated with Eq. [6] if the spectral transmittance of the pyrgeometer dome is available, along with spectra for the radiation source used during calibration

and radiation source being measured. Data from Fig. 12 and a spectral response for a silicon dome were input into Eq. [6] to provide an estimate of pyrgeometer spectral error for clear and overcast sky conditions. If error for measurement of a blackbody (overcast sky) was assumed to be zero, spectral error for clear sky results in low measurements by approximately 2%. This is a theoretical value. Differences between LW_i measurements from field calibrated pyrgeometers and an absolute sky scanning radiometer have been reported as less than 2 W m^{-2} for nighttime conditions (Marty et al., 2003; Philipona et al., 2001), indicating small spectral errors for spectral differences between clear and cloudy skies.

Net Radiometer Designs

Instruments designed to measure R_n are called net radiometers. There are four basic designs of net radiometer. The most complex is a four-component net radiometer (e.g., Apogee Instruments model SN-500, EKO Instruments model MR-60, Hukseflux model NR01, Kipp & Zonen model CNR 4), which consists of four individual radiometers (upward-looking pyranometer, downward-looking pyranometer, upward-looking pyrgeometer, and downward-looking pyrgeometer) to independently measure the four components of R_n (SW_i, SW_o, LW_i, and LW_o). The radiometers are usually mounted in a single housing, but a four-component net radiometer can be assembled by deploying individual radiometers to measure SW_i, SW_o, LW_i, and LW_o at the same location. The information in preceding sections regarding shortwave and longwave irradiance measurements applies directly to pyranometers and pyrgeometers used in four-component net radiometers.

A net radiometer model similar to a four component instrument consists of four independent blackbody absorbers, but only two thermopiles, one for SW_n mounted between the upward- and downward-looking shortwave absorbers and one for LW_n mounted between the upward- and downward-looking longwave absorbers (e.g., Kipp & Zonen model CNR 2, which was discontinued in 2011). A challenge with this type of net radiometer design is matching the upward- and downward-looking detectors (combination of filter, absorber, and detector plate) so sensitivity is equal. If sensitivities of upward- and downward-looking detectors are not equal, then changing proportions of SW_i and SW_o, and LW_i and LW_o, will cause errors in measurements of SW_n and LW_n, respectively.

An instrument that measures all wavelengths, shortwave and longwave, incident on the absorber is called an all-wave radiometer or pyrradiometer (e.g., Philipp Schenk model 240–8111). Pyrradiometers consist of a blackbody surface and thermopile covered by a dome that transmits shortwave and longwave radiation (typically polyethylene). Thus, another type of net radiometer is the combination of an upward-looking pyrradiometer and downward-looking pyrradiometer, which independently measure incoming all-wave irradiance and outgoing all-wave irradiance. A challenge with this type of net radiometer is unequal dome transmittance for shortwave and longwave radiation. If dome transmittance is not equal for shortwave and longwave radiation, changing proportions of shortwave and longwave cause measurement errors.

The simplest type of net radiometer is a net all-wave radiometer, sometimes called a net pyrradiometer, which consists of a single thermopile fitted between two blackbody absorbers, one upward-looking and one downward-looking (e.g., EKO Instruments model MF-11, Hukseflux model NR02, Kipp & Zonen model NR Lite2, Radiation and Energy Balance Systems (REBS) model Q*7.1). The thermopile

produces a voltage proportional to the difference between incoming and outgoing all-wave irradiance (temperature difference between upward- and downward-looking detectors). The challenges of matching detectors and unequal transmittance of shortwave and longwave radiation apply to net all-wave radiometers.

The energy balance of detector plates in pyrradiometers and net pyrradiometers is dependent on the shortwave and longwave transmittance of the domes and shortwave and longwave absorptance of the detector surface. Theoretically, transmittance and absorptance should be 100% for all wavelengths. Differences in transmittance and absorptance, particularly differences in shortwave and longwave transmittance and absorptance, will cause errors with changes in irradiance spectra (e.g., clear versus cloudy sky, day versus night). Measurements of shortwave and longwave transmittance of multiple different polyethylene domes revealed lower longwave transmittance relative to shortwave transmittance in every case (Campbell and Diak, 2005). On average, transmittance of longwave was lower than shortwave by 14% (range was 4 to 25%), with greater differences for thicker domes. One solution is to use thinner domes, but they are not as rugged and may require more maintenance. Matching upward- and downward-looking detectors for a net pyrradiometer is also challenging. If sensitivity of the two detectors is not matched, changing proportions of incoming and outgoing radiation will cause errors in measurement of R_n.

Net Radiometer Comparisons

In the most recent net radiometer study we are aware of, Blonquist et al. (2009a) compared five different net radiometer models (Kipp & Zonen model CNR 1, Hukseflux model NR01, Kipp & Zonen model CNR 2, Kipp & Zonen model NR Lite, and Radiation and Energy Balance Systems model Q*7.1) in the field. There is not a standard for R_n measurement, so the means of measurements from the four-component net radiometers (Kipp & Zonen model CNR 1 and Hukseflux model NR01) were used to calculate reference R_n and was used for comparison of all individual radiometers. Measurements of SW_i and LW_o from the four-component radiometers closely matched independent reference measurements (SW_i from a Kipp & Zonen model CM 11 pyranometer and LW_o from an Apogee Instruments model SI-111 infrared radiometer). Measurements of SW_i were typically within 1% of the reference (except at low solar zenith angles) and measurements of LW_o were typically within 2% of the reference (see Fig. 14 in Surface Temperature section). Duchon and Wilk (1994) also compared downward-looking pyrgeometers to an infrared radiometer and found close agreement. In addition to comparing radiometers to reference SW_i and LW_o, Blonquist et al. (2009a) flipped all radiometers during the day (near solar noon on a clear day) and found the SW_o and LW_i radiometers matched SW_i and LW_o radiometers within 1% in all cases but one (which was approximately 2%). Based on these results, it was judged that R_n calculated from mean component measurements from the four-component net radiometers was a reasonable R_n measurement for use as reference R_n.

Blonquist et al. (2009a) reported that four-component net radiometers were the most accurate under all conditions (day, night, clear, cloudy). A difference of approximately 5% in LW_i measurements from the Kipp & Zonen CNR 1 and Hukseflux NR01 radiometers was measured, likely due to differences in calibration procedures used by manufacturers. In a similar net radiometer study, Brotzge and Duchon (2000) also found differences between longwave measurements. As

detailed earlier, different techniques are available to calibrate pyrgeometers and yield different results depending on how radiometer spectral response is accounted for (Gröbner and Los, 2007). In a round-robin pyrgeometer calibration experiment, some laboratories derived the same calibration factors (within limits of uncertainty) and other laboratories did not (Philipona et al., 1998). Differences in SW_i, SW_o, and LW_o from the two four-component net radiometer models were typically 1 to 2%. Michel et al. (2008) found larger error in shortwave measurements than longwave measurements when comparing four-component net radiometers.

Blonquist et al. (2009a) found the two net all-wave radiometers (Kipp & Zonen model NR-Lite and REBS model Q*7.1) were the least accurate, and the Kipp & Zonen model CNR 2 (discontinued in 2011) was intermediate in accuracy. Net all-wave radiometers tended to measure R_n approximately 2 to 4% low during the day and approximately 15 to 30% low in magnitude at night. Others have reported similar low readings relative to four-component R_n measurements (Brotzge and Duchon, 2000; Cobos and Baker, 2003). Both models were less sensitive to longwave than shortwave, by approximately 20% and 30% for the NR-lite and Q*7.1, respectively. Others have also reported lower longwave sensitivity for net all-wave radiometers (Brotzge and Duchon, 2000; Cobos and Baker, 2003; Duchon and Wilk, 1994; Field et al., 1992; Halldin and Lindroth, 1992). This means the radiometers will be most accurate under conditions similar to conditions during calibration and error will increase as proportions of shortwave and longwave radiation deviate from those during calibration. This explains why both radiometers measured low in magnitude at night, as there is no shortwave radiation at night. Others have measured differences between clear and cloudy skies (Cobos and Baker, 2003; Field et al., 1992). Separate calibrations for day and night have been proposed (Brotzge and Duchon, 2000; Fritschen and Fritschen, 2007), and others have recommended field calibration of net all-wave radiometers under conditions similar to those the radiometers will be used in (Halldin and Lindroth, 1992; Kustas et al., 1998).

Sensitivities of upward- and downward-looking detectors were less than 1% different for all NR Lite radiometers, but upward-looking detectors were approximately 3% more sensitive than downward-looking detectors on all Q*7.1 radiometers (Blonquist et al., 2009a). This may have been due to increased exposure to shortwave for upward-looking detectors, as matching of detectors wasn't measured until after radiometers had been deployed in the field for a few weeks. Similar to differential sensitivity to shortwave and longwave radiation, differential sensitivity between upward- and downward-looking detectors results in error when proportions of incoming and outgoing radiation are significantly different than those during calibration (e.g., plant canopy surface compared to snow covered surface). Results from the CNR 2 highlight the importance of matching upward- and downward-looking detectors. Two of the three CNR 2 SW_n radiometers had mismatched detectors, on the order of 6 to 8%. This did not lead to large errors when the radiometers were deployed over a vegetated surface, indicating calibration conditions were similar to a vegetated surface. However, when going from a vegetated surface (albedo near 0.20) to a snow surface (albedo near 0.80), detector mismatching of 5 to 10% leads to SW_n errors in the range of 20 to 40%. Errors are highly dependent on albedo and get worse as albedo increases. Mismatching of the longwave detectors on the CNR 2 was much lower, approximately 2%. This would yield much smaller LW_n errors, as relative proportions of LW_i and

LW_o typically don't change as much as relative proportions of SW_i and SW_o when going from one surface (or sky) condition to another.

The NR Lite net radiometers were extremely sensitive to precipitation and dew and/or frost on the detectors because the detectors are unshielded (Blonquist et al., 2009a). Thus, energy balance of the detector is altered by the presence of water. Data collected when detector surfaces were wet were not accurate. Others have reported this as well (Brotzge and Duchon, 2000; Cobos and Baker, 2003). Wind also influences the energy balance of the detector surfaces and causes errors if not accounted for (Brotzge and Duchon, 2000; Cobos and Baker, 2003; Fritschen and Fritschen, 2007). The NR Lite and Q*7.1 net radiometers have manufacturer-supplied wind speed correction equations that should be applied.

Since the net radiometer comparison of Blonquist et al. (2009a), Kipp & Zonen upgraded the CNR 1 to the CNR 4 and the NR Lite to the NR Lite2. Improvements in the CNR 4 are a curved dome and better thermal coupling on the upward-looking pyrgeometer, reference temperature sensor placed closer to pyrgeometer detectors, solar shield, and lighter weight. A heating and ventilation unit is now available as a built-in option. Halldin and Lindroth (1992) recommended heating and ventilation under all conditions. Malek (2008) found unheated and unventilated net radiometers measured higher than a heated and ventilated unit when dew/frost was on the domes (enhancing LW_i), but lower when snow covered the domes (reducing SW_i). Michel et al. (2008) found that a heated and ventilated CNR 1 net radiometer did not match a four-component Eppley system in the field, but could be field calibrated to match. Improvements in the NR Lite2 are refinements to specifications. In addition, other net radiometers, beyond those compared by Blonquist et al. (2009a), are available and some new net radiometers have been released since the field data were collected in 2007.

Rather than serve as a comprehensive review of all available instruments, information contained in this section should serve as a guide to users regarding strengths and weaknesses of instrument types, and challenges of making R_n measurements with any instrument. To summarize, four-component net radiometers provide the most information, but the disadvantage is high cost and requirement of multiple datalogger channels (at least five differential channels) to make the measurements. Paired all-wave radiometers and net all-wave radiometers are lower cost than four-component instruments for measuring R_n, but they are subject to sources of error that typically make them less accurate than four-component instruments. In addition, detectors (combination of domes, absorbing surfaces, and detector plates) may have different sensitivities to shortwave and longwave radiation. Mismatching of upward-looking and downward-looking detectors can also cause errors in net all-wave radiometers. Blonquist et al. (2009a) concluded that R_n measurements from four-component net radiometers are the most accurate, assuming accurate calibration of individual radiometers, and are preferred over other R_n measurement methods (as long as cost is not limiting). Similar conclusions have been reported in other studies comparing R_n from four-way net radiometers and net all-wave radiometers (Kohsiek et al., 2007).

Modeling Net Radiation

Due to the cost of net radiometers, and in some cases number of datalogger channels required to make measurements with net radiometers, R_n is often modeled. Perhaps the most common application of R_n modeling is in evapotranspiration

(ET) prediction from automated weather stations, as R_n is one of the primary drivers of ET, but it is uncommon to find an ET weather station with a net radiometer. Most R_n models use a measurement of SW_i from a pyranometer, an assumed (typically constant) value of albedo to calculate SW_o from SW_i, and air temperature, humidity, and cloudiness measurements/estimates to estimate LW_n. An example of this approach is the R_n sub-model in the ASCE Standardized Reference Evapotranspiration Equation (ASCE-EWRI, 2005). Comparison of R_n modeled with this approach to measured R_n indicated R_n measurements from multiple net radiometer models were more accurate than R_n estimates from this particular R_n prediction model (Blonquist et al., 2010; Blonquist et al., 2009a).

A better approach to model R_n for vegetated surfaces may be to measure SW_i, estimate albedo from a simple plant canopy radiative transfer model (Campbell and Norman, 1998), measure surface temperature with an IR radiometer from which LW_o can be calculated (see next section), and estimate LW_i with a prediction model. While the albedo estimate requires some lengthy equations, it yields a temporally variable albedo for clear sky conditions, consistent with measured values. Measurement of LW_o (from surface temperature measurement) eliminates the need to model LW_n ($LW_i - LW_o$), which was found to be the largest source of error in a common R_n model (Blonquist et al., 2010), in favor of estimating only the LW_i component of LW_n from a model. Multiple LW_i models have been evaluated and assessed for accuracy relative to LW_i measurements (Flerchinger et al., 2009).

Surface Temperature

Radiometers used to remotely measure surface temperature are often called infrared thermometers (IRTs) (e.g., Apogee Instruments model SI-111, Everest Interscience model ENVIRO-THERM), but infrared radiometer (IRR) is a better descriptor because thermal infrared radiation emitted from the surface of interest is being detected and then converted to surface temperature (Huband, 1985a). Infrared radiometers function exactly the same way as pyrgeometers, where the output signal is dependent on the longwave radiation balance of the detector (difference between absorbed and emitted longwave radiation). The difference between an IRR and pyrgeometer is the filter and field of view. Pyrgeometers have a wide field of view (150°-180°), whereas IRRs typically have a narrow field of view (60° or less). Pyrgeometers have a filter sensitive to broad range (4.5 to 50 μm), whereas IRRs have a filter that is only sensitive to a narrow range of wavelengths within the thermal infrared range. IRRs should have filters that approximate the so-called atmospheric window, the wavelength range where the atmosphere is relatively transparent to thermal infrared radiation, typically defined as 8 to 14 μm (Fig. 13). Between 8 and 14 μm air molecules emit and absorb little thermal infrared radiation. As a result, IRRs 'see through' the atmosphere and sense radiation emitted by the surface.

As with pyrgeometers, the signal output from an IRR is proportional to the incoming longwave radiation absorbed by the detector and the longwave radiation emitted by the detector. With IRRs, temperature is the desired quantity, rather than radiation, thus Eq. [9] is written in terms of temperature using the relationship between radiation emission and temperature (Stefan–Boltzmann Law) (Fuchs and Tanner, 1966; Kalma et al., 1988):

$$CF = \frac{\sigma T_T^4 - \sigma T_D^4}{S} \qquad [11]$$

where T_T is target temperature and σT_T^4 is radiation emitted by the target and absorbed by the detector, T_D is detector temperature and σT_D^4 is radiation emitted by the detector, and CF is a calibration factor determined during radiometer calibration. Calibration of IRRs is typically done by the manufacturer, where a blackbody or near blackbody radiation source of known temperature is used to provide a range of T_T values for different values of T_D (Fuchs and Tanner, 1966; Amiro et al., 1983; Huband, 1985b; Kalma et al., 1988). Following calibration, subsequent surface temperature measurements are made by rearranging Eq. [11] to solve for T_T and inputting measurements of S and T_D.

Unless the surface being measured is a blackbody (ε = 1), target temperature (T_T in Eq. [11]) measured by an IRR is an apparent surface temperature, often called brightness temperature, which can be thought

Fig. 13. Atmospheric transmittance from 5 to 20 μm. The atmospheric window is typically defined as the range from 8 to 14 μm. These data were modeled with MODTRAN assuming a typical mid-latitude summer atmosphere at a distance of two meters from the surface (two meters represents a typical IRR mounting height above the surface). At wavelengths less than 8 μm, water vapor (H_2O) absorption and emission can cause interference, and at wavelengths greater than 14 μm carbon dioxide (CO_2) absorption and emission can cause interference.
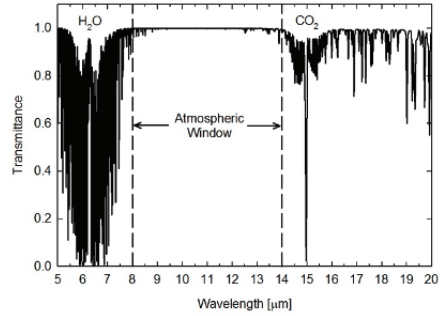
of as temperature of a blackbody emitting the same radiance as that observed by the radiometer (Norman and Becker, 1995). Actual surface temperature of the elements within the field of view of the radiometer, called radiometric temperature, is determined by making a correction for the influence of surface emissivity. Thermal infrared radiation incident on the radiometer detector (σT_B^4) includes radiation emitted by the surface (σT_R^4) and reflected radiation from the background (σT_{Sky}^4):

$$\sigma T_B^4 = \varepsilon \sigma T_R^4 - (1-\varepsilon) \sigma T_{Sky}^4 \qquad [12]$$

where T_B is brightness temperature (K), T_R is surface radiometric temperature (K), and T_{Sky} is sky temperature (K) in the 8 to 14 μm wavelength range. Radiation emitted by the surface is usually a large fraction, equal to surface ε, of total radiation incident on the detector because most terrestrial surfaces are nearly blackbodies (Table 4).

Radiation reflected from the background is a small fraction of total radiation, equal to 1 - ε. In outdoor settings, background radiation is sky radiation in the 8 to 14 μm range. Sky temperature in the 8 to 14 μm range is far colder than surface temperature on clear days, thus the small reflected fraction from the background can have a large impact on radiometric temperature and must be accounted for. It can be measured by directing an IRR toward the sky, or it can be predicted with a model (Idso, 1981; Kimball et al., 1982). We have successfully used a simple model derived for the high-elevation, semiarid climate in Logan, UT:

$$T_{Sky} = T_{Air} + 50 f_{Clouds} - 60 \qquad [13]$$

Table 4. Emissivities (ε, broadband longwave emittance) for some terrestrial and man-made surfaces (Campbell and Norman, 1998).

Surface	Emissivity (ε)
Plant leaves	0.94–0.99
Soil	0.93–0.96
Water	0.96–0.98
Concrete	0.88–0.93
Aluminum foil	0.06

where T_{Air} is air temperature (K) and f_{Clouds} is fraction of cloud cover. The coefficients 50 and 60 in Eq. [13] may not be representative of all climates, but can be determined for a given location by simultaneous measurement or estimation of T_{Sky}, T_{Air}, and f_{Clouds}.

By rearranging Eq. [12], the influence of surface ε and reflected radiation from the background can be corrected, if ε and background (sky) temperature are measured or estimated:

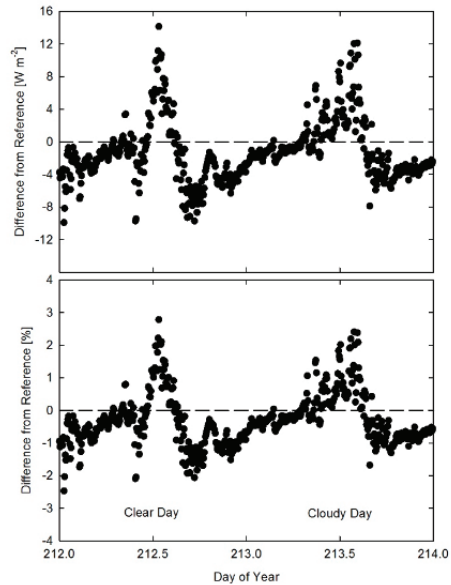$$T_R = \sqrt[4]{\frac{T_B{}^4 - (1-\varepsilon) T_{Sky}{}^4}{\varepsilon}} \tag{14}$$

where T_T determined from Eq. [11] is input as T_B. Equations [12] and [14] assume constant ε at all wavelengths, an infinite wavelength range for radiation emission, and equal sensitivity to all wavelengths for the IRR. These assumptions are not strictly valid, as wavelength ranges measured by IRRs are typically close to the atmospheric window of 8 to 14 μm, IRR sensitivity is not equal across all wavelengths, and ε varies with wavelength for some surfaces. However, Eq. [14] is a reasonable approximation because background radiation is a small fraction (1- ε) of total radiation for land surfaces and ε varies little with wavelength with the 8 to 14 μm range for most land surfaces (soils with significant amounts of quartz are an exception). IRRs should have highly uniform sensitivity to wavelengths within the 8 to 14 μm range.

To demonstrate the importance of accounting for reflected background radiation, some typical values can be input into Eq. [14]. For a full cover plant canopy, ε is higher than that for individual leaves, and is often 0.97 to 0.99 (Fuchs and Tanner, 1966; Campbell and Norman, 1998). On a clear day, $T_B = 25$ °C and $T_{Sky} = -40$ °C are reasonable values. Assuming $\varepsilon = 0.98$, then $T_R = 25.95$ °C, nearly a whole degree warmer than T_B (apparent surface temperature). On a cloudy day, $T_B = 25$ °C and $T_{Sky} = 15$ °C are reasonable values. Again assuming $\varepsilon = 0.98$, then $T_R = 25.19$ °C, much closer to T_B. The difference between T_R and T_B will be larger if emissivity is smaller and if the difference between T_B and T_{Sky} is larger. If T_B and T_{Sky} are equal, T_R is also equal and correction for reflected background radiation is not necessary, but this only occurs on very cloudy or overcast days.

Sometimes an emissivity correction is applied where signal returned by an IRR is divided by surface emissivity, and some IRRs have an emissivity dial that makes this adjustment. Campbell and Diak (2005) suggested this type of correction is a holdover from days when IRRs were used to determine temperature of molten metal in furnaces. However, this correction does not account for reflected radiation and should not be used to calculate radiometric temperature in environmental applications, thus the emissivity dial should be set to 1.00. Under clear sky conditions,

this correction reduces error relative to no correction for emissivity, but under cloudy conditions it may cause larger error than no emissivity correction. These effects are shown graphically in Appendix B of Blonquist et al. (2009b).

Infrared radiometers directed toward Earth's surface can be used as pyrgeometers because terrestrial surfaces are approximately blackbody emitters. Thus, T_T from Eq. [11] can be input into the Stefan–Boltzmann equation, along with ε equal to one, to calculate LW_o. If the surface is not uniform, LW_o from the IRR will be representative of the surface elements within the field of view of the IRR (IRRs typically have much narrower fields of view than pyrgeometers). Data comparing LW_o from an IRR (Apogee Instruments model SI-111) and pyrgeometer (Kipp & Zonen model CGR 3) for a clear and cloudy day over turfgrass in Logan, UT, indicate differences less than 3% (Fig. 14). IRRs with a filter that approximates the atmospheric window cannot be directed toward the sky

Fig. 14. Difference [in absolute units (W m⁻²), top graph, and relative units (%), bottom graph] in outgoing longwave radiation calculated from surface temperature measured with an infrared radiometer (Apogee Instruments model SI-111) relative to a pyrgeometer (Kipp & Zonen model CGR 3). Day of year 212 was a clear day and day of year 213 was a cloudy day.

and used as pyrgeometers. Sky temperature measured within this wavelength range will be much colder than actual sky temperature, thus LW_i calculated from this sky temperature will be much lower than actual LW_i.
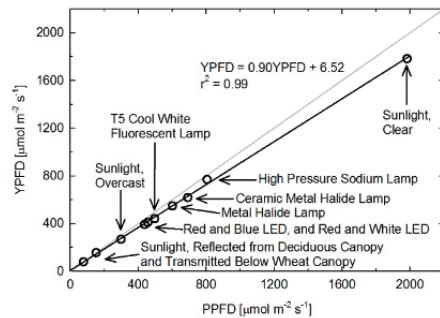
Photosynthetically Active Radiation

Photosynthetically active radiation (PAR) is the subset of shortwave radiation that drives photosynthesis. PAR should be quantified in units that express number of photons (photon flux density) rather than energy content of radiation (energy flux density) because one photon excites one electron (Stark–Einstein Law) in chlorophyll molecules in plant leaves, independent of the energy of the photon (energy content of photons is dependent on wavelength, with photons of shorter wavelength having higher energy, see Eq. [2]). As a result, equal energy flux densities of radiation of different wavelengths will not yield equal photon flux densities.

Instantaneous PAR is typically reported as photon flux density in units of micromoles of photons per square meter of area per second (μmol m⁻² s⁻¹) between 400 and 700 nm. Daily total PAR is typically reported in units of moles of photons per square meter per day (mol m⁻² d⁻¹) between 400 and 700 nm, and is often called daily light integral (DLI).

Photosynthesis does not respond equally to all photons due to the combination of spectral absorptivity of plant leaves (absorptivity is higher for blue and red
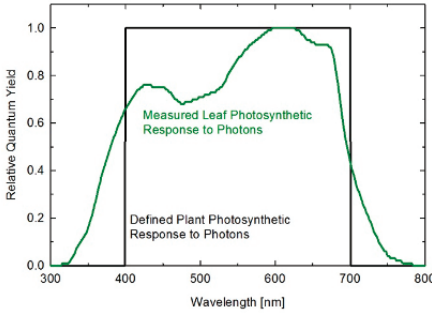
Fig. 15. Measured single leaf relative quantum yield and defined plant relative quantum yield. Quantum yield is moles of carbon fixed per mole of photosynthetic photons absorbed. Relative quantum yields were calculated by normalizing to maximum values giving the relative photosynthetic response photons, which can be thought of as photosynthetic efficiency. Single leaf measurements were made at low intensity in monochromatic radiation and the plot shown is the mean of 22 species of plants grown in the field [from McCree (1972a); Inada (1976) derived a similar curve with data from 33 species, but with a narrower blue peak and broader red peak]. The defined relative plant photosynthetic response to photons gives equal weight to all photons between 400 and 700 nm, a somewhat arbitrary, but simpler and almost universally used, definition.

Fig. 16. Correlation between photosynthetic photon flux density (PPFD) and yield photon flux density (YPFD) for multiple radiation sources. Yield photon flux density is about 90% of PPFD. Spectral photon flux density measurements were made with a spectroradiometer (Apogee Instruments model PS-200) and appropriate weighting factors were used to calculate PPFD (defined plant photosynthetic response to photons in Fig. 15) and YPFD (measured leaf photosynthetic response to photons in Fig. 15).

photons than green photons) and absorption of PAR by nonphotosynthetic pigments. In monochromatic radiation, photons from approximately 600 to 630 nm are the most efficient (Fig. 15) (McCree, 1972a; Inada, 1976). One potential definition of PAR is weighting photon flux density (μmol m^{-2} s^{-1}) at each wavelength between 300 and 800 nm by relative quantum yield (quantum yield is moles of carbon fixed per mole of photosynthetic photons absorbed; relative quantum yield is calculated by normalizing by the maximum value) measured in monochromatic radiation and summing the result. This is called yield photon flux density (YPFD) (μmol m^{-2} s^{-1}) (Sager et al., 1988). This definition, however, is not generally appropriate for broad spectrum radiation sources over longer time intervals in whole plants. Measurements used to generate the relative quantum yield data were made on single leaves under low intensity monochromatic radiation levels and at short time scales (McCree, 1972a; Inada, 1976). Whole plants and plant canopies have multiple leaf layers and photosynthetic pigments may adapt to their radiation environment. Also, relative quantum yield shown in Fig. 15 is the mean from 22 species grown in the field (McCree, 1972a); there was some variability between species (McCree, 1972a; Inada, 1976). In addition, mean relative quantum yield for the same species grown in growth chambers was similar, but there were significant differences at shorter wavelengths less than 450 nm.

McCree (1972b) found that equally weighting all photons between 400 and 700 nm and summing the result, defined as photosynthetic photon flux density (PPFD) (μmol m^{-2} s^{-1}), was well

correlated to photosynthesis, and was similar to correlation between YPFD and photosynthesis. As a matter of practicality, PPFD is a simpler definition of PAR, and it is easier to construct a sensor with spectral response that matches PPFD weighting factors. At the same time as McCree's work, others had proposed PPFD as an accurate measure of PAR and built sensors that approximated the PPFD weighting factors (Biggs et al., 1971; Federer and Tanner, 1966). Correlation between PPFD and YPFD measurements for several radiation sources is very high (Fig. 16). As an approximation, YPFD = 0.90*PPFD. Based on all these factors, PAR is almost universally defined as PPFD rather than YPFD. The only radiation sources shown in Fig. 16 that don't fall on the regression line are the high pressure sodium (HPS) lamp, reflection from a plant canopy, and transmission below a plant canopy. A large fraction of radiation from HPS lamps is in the red range of wavelengths where the YPFD weighting factors are at or near one. The factor for converting PPFD to YPFD for HPS lamps is 0.95, rather than 0.90. The factor for converting PPFD to YPFD for reflected and transmitted photons is 1.00.
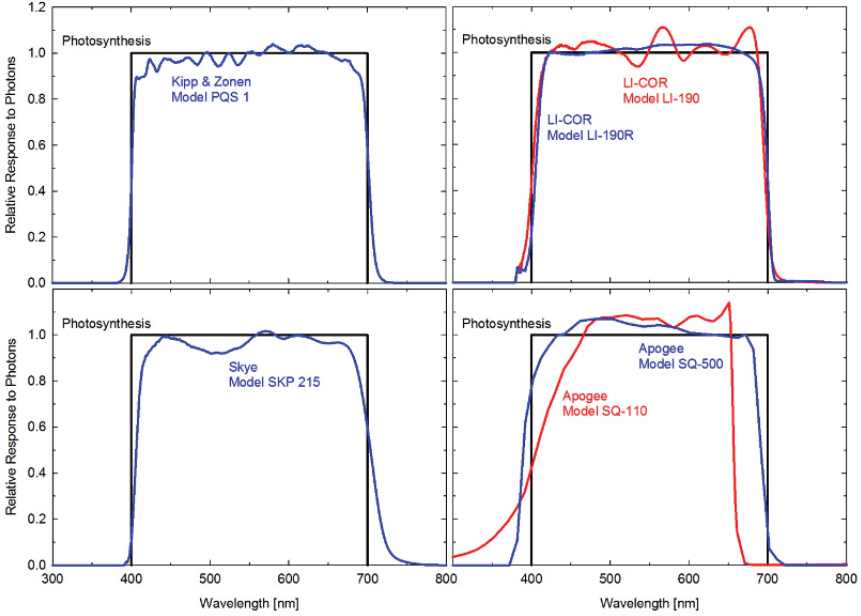
Quantum Sensors

The simplest and most common way to measure PPFD is with a quantum sensor (e.g., Apogee Instruments model SQ-500, EKO Instruments model ML-020P, Kipp & Zonen model PQS 1, LI-COR model LI-190R, Skye Instruments model SKP 215), so called because a photon is a single quantum of radiation. Quantum sensors are also called PAR sensors, which is a more intuitive name. Standard quantum sensors consist of a combination of a photodetector, interference filter(s), and diffuser, all mounted in a weatherproof housing. The photodetector is often a silicon-cell photodiode, but other photodetectors have been used (Mims, 2003; Pontailler, 1990). The major difference between a quantum sensor and silicon-cell pyranometer is the interference filter. The purpose of the filter is to provide equal response to photons between 400 and 700 nm and block photons outside this range [filter(s) matches sensor response to defined plant photosynthetic response to photons shown in Fig. 15].

Quantum sensors designed for measuring PPFD underneath plant canopies are called line quantum sensors. Line quantum sensors provide an average PPFD measurement along the length of a bar (line) where multiple detectors or a single linear diffuser and light transmission mechanism are mounted. An average PPFD measurement along a line is highly beneficial underneath plant canopies because they are heterogeneous, making light transmission and under-canopy PPFD nonuniform.

The combination of diffuser transmittance, interference filter(s) transmittance, and photodetector sensitivity yields spectral response of a quantum sensor. A perfect photodetector, filter, and/or diffuser combination would exactly reproduce the defined plant photosynthetic response to photons (Fig. 15), but this is challenging in practice. Mismatch between the defined plant photosynthetic response and sensor spectral response results in spectral error when the sensor is used to measure radiation from sources with a different spectrum than the radiation source used to calibrate the sensor (Federer and Tanner, 1966; Ross and Sulev, 2000). This concept is exactly the same as spectral error resulting from the imperfect spectral response of a silicon-cell pyranometer.

To demonstrate spectral errors, spectral responses of six models of quantum sensors (Apogee Instruments models SQ-110 and SQ-500, Kipp & Zonen model PQS 1, LI-COR models LI-190 and LI-190R, Skye Instruments model SKP 215;

Fig. 17. Relative spectral response (quantum sensor response is signal output by the sensor per μmol of photons incident on the sensor, and relative responses were derived by normalizing by a mean value calculated from data in the 400 and 700 nm range) of six models of quantum sensors (Apogee Instruments models SQ-110 and SQ-500, Kipp & Zonen model PQS 1, LI-COR models LI-190 and LI-190R, Skye Instruments model SKP 215,) compared to the defined plant photosynthetic response to photons (labeled photosynthesis). Sensor spectral response data were used to calculate spectral errors with Eq. [15] (Table 5). Sensor spectral response data were obtained from manufacturers.

spectral response data were provided by sensor manufacturers) were compared to the defined plant photosynthetic response to photons (Fig. 17). The quantum sensor models are designed to provide equal weighting to photons between 400 and 700 nm and block photons outside this range, but they deviate by as much as ± 10% at certain wavelengths and don't have exact cutoffs at 400 and 700 nm. As with silicon-cell pyranometers, spectral error can be quantified for any quantum sensor used to measure any radiation source as long as sensor spectral response (S_λ), calibration source spectral output ($I_{\lambda Calibration}$), and measured radiation source spectral output ($I_{\lambda Measurement}$) are known (Federer and Tanner, 1966; Ross and Sulev, 2000):

$$\text{Error} = \frac{\int S_\lambda I_{\lambda Measurement} d\lambda \int_{400}^{700} I_{\lambda Calibration} d\lambda}{\int S_\lambda I_{\lambda Calibration} d\lambda \int_{400}^{700} I_{\lambda Measurement} d\lambda} \qquad [15]$$

where the integral from 400 to 700 is for the defined plant photosynthetic response to photons. Spectral errors for different radiation sources were calculated with Eq. [15] for the quantum sensor spectral responses shown in Fig. 17 (Table 5). Data indicate errors typically less than 3% for sunlight in multiple conditions (clear, cloudy, reflected from plant canopies, transmitted below plant canopies) and common broad spectrum electric lamps (cool white fluorescent, metal halide,

high pressure sodium), but errors tend to be larger for single color (narrowband) light emitting diodes (LEDs), and mixtures of LEDs. Barnes et al. (1993) reported similar results for direct comparison of quantum sensor measurements of PPFD to PPFD measurements from a spectroradiometer. For the best spectral accuracy, Barnes et al. (1993) suggested calibrating quantum sensors against a spectroradiometer for specific radiation sources.

In addition to spectral errors, quantum sensors have the same errors discussed for pyranometers (calibration error, directional error, temperature sensitivity, long-term stability, general use error). To evaluate these errors, approximately two and half years of continuous data were collected for replicates of three models of quantum sensors (Apogee Instruments model SQ-110, Kipp & Zonen model PQS 1, and LI-COR model LI-190) deployed outside in Logan, UT. There is not a reference standard for PAR measurements, so the mean of two replicates of each quantum sensor was used as a reference for comparison. Relative to this reference PPFD, angular differences were typically less than 3% for solar zenith angles between 20° and 60°, and less than 6% at a solar zenith angle of 75°. Drift rates for all sensors deployed on the rooftop, relative to the reference PPFD, were less than 1% per year (except for one LI-190, which appeared to be influenced by moisture intrusion).

Table 5. Relative spectral errors (%) for six models of quantum sensors (Apogee Instruments models SQ-110 and SQ-500, Kipp & Zonen model PQS 1, LI-COR models LI-190 and LI-190R, Skye Instruments model SKP 215) for multiple radiation sources.

Radiation Source	Kipp & Zonen Model PQS 1	LI-COR Model LI-190	LI-COR Model LI-190R	Skye Model SKP 215	Apogee Model SQ-110‡	Apogee Model SQ-500
Sunlight						
Clear sky†	0.0	0.0	0.0	0.0	0.0	0.0
Overcast sky	-0.2	0.0	-0.2	-0.4	1.4	0.5
Reflected from grass canopy	1.8	0.3	1.5	6.6	5.7	0.0
Transmitted below wheat canopy	0.6	0.3	0.7	4.1	6.4	1.1
Common electric lamps						
Cool white fluorescent, T5	1.1	0.1	1.6	0.2	0.0	2.2
Metal halide	-0.1	0.3	0.3	-2.1	-3.7	3.1
Ceramic metal halide	0.5	0.6	1.5	-0.3	-6.0	1.9
High pressure sodium	2.3	0.9	2.9	1.5	0.8	2.2
Light emitting diodes (LEDs)						
Blue (448 nm peak)	-2.2	2.0	-0.4	0.8	-12.7	3.0
Green (524 nm peak)	-1.0	-1.6	2.0	-3.1	8.0	5.2
Red (635 nm peak)	2.7	0.9	3.4	0.7	4.8	0.2
Red (668 nm peak)	-1.1	4.5	0.5	-1.4	-79.1	-1.9
Red and blue mix (84% Red,16% Blue)	-1.1	3.8	0.5	-1.1	-65.3	-1.2
Red and white mix (79% Red, 21% White)	-1.0	3.6	0.7	-1.4	-60.3	-0.8
Cool white fluorescent	0.2	1.2	1.8	0.3	-4.6	2.2

† Sunlight under clear sky conditions was used as the reference ($I_{ICalibration}$ from Eq. [15]).

‡ Assumes separate calibrations for sunlight and electric light (T5 cool white fluorescent was used as electric light calibration reference).

Temperature response from the rooftop data was difficult to measure due to simultaneous changes in solar zenith angle, sky conditions (degree of cloudiness), and temperature. The quantum sensor models have temperature sensitivity specifications ranging from -0.15 to 0.15% per °C. The data suggested that all of the sensors met their temperature sensitivity specifications. Subsequently, temperature sensitivity for three quantum sensor models (Apogee Instruments models SQ-110 and SQ-500, LI-COR model LI-190) was measured by placing them underneath a radiation source (cool white fluorescent LED bulb) inside a temperature controlled chamber and varying the temperature across a wide range (-20 to 50 °C). Data were collected at multiple temperature steps across the range, and at each temperature sensors were allowed to equilibrate for thirty minutes. Reference radiation intensity was measured with a spectroradiometer (Apogee Instruments model PS-200) mounted outside the temperature chamber to keep it at room temperature (only the sensing head and fiber optic cable were placed inside the temperature chamber). Two of the sensor models (LI-190 and SQ-500) had negative slopes (signal decreased as temperature increased) and were less than -0.1% per °C, within specifications provided by manufacturers. This is the expected result based on inference from the wavelength-dependent temperature sensitivity of silicon cells (Fig. 8), where the temperature coefficient is negative for all wavelengths measured by the quantum sensors. Most quantum sensors have relatively uniform sensitivity from 400 to 700 nm. The temperature coefficient of silicon is relatively uniform and near zero from 500 to 700 nm, but is negative at all wavelengths less than 500 nm. This means quantum sensors built with silicon-cell photodiodes should have negative and small temperature sensitivity (less than -0.1% per °C), unless the radiation source being measured outputs a significant amount of blue radiation (wavelengths less than 500 nm). The other model (SQ-110) is not constructed with a silicon-cell photodiode, but uses a gallium arsenide phosphide photodetector, and had a small positive slope (less than 0.1% per °C).

Spectroradiometers

While quantum sensors are typically used to measure PPFD, spectroradiometers have the potential to be the most accurate PPFD sensors because they separate radiation into individual wavelengths and independently measure intensity at multiple wavelengths within the range of interest, in this case the defined PAR range. The major drawback of spectroradiometers is cost, which is approximately an order of magnitude higher than quantum sensors. A few hundred dollars is common for quantum sensors, whereas a few thousand dollars is common for spectroradiometers. However, for radiation sources with unique spectra, such as LEDs with narrowband output, spectroradiometers are often used to measure PPFD because of better spectral accuracy. The main components of spectroradiometers are a prism or diffraction grating to separate radiation into individual wavelengths, a detector or detector array to measure radiation intensity of the different wavelengths, and circuitry to digitize the signal. Spectral errors of quantum sensors (Table 5) are eliminated when measuring PPFD with a spectroradiometer. All other sources of error (imperfect directional response, temperature sensitivity, etc.) must still be considered and will be dependent on the specific spectroradiometer model used to measure PPFD. Spectroradiometers can also be used to measure YPFD by multiplying photon flux density measurements by measured leaf photosynthetic response weighting factors (Fig. 15) and summing the result. As previously indicated, YPFD measurements may not be appropriate for broadband radiation sources and are not commonly made or reported.
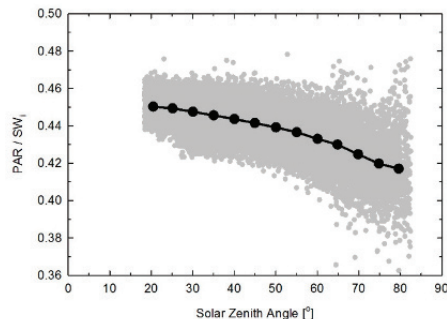
Modeling Photosynthetically Active Radiation

Quantum sensors are widely available and relatively inexpensive, thus measurement of PPFD is common, particularly in laboratories, greenhouses, growth chambers, and at flux tower sites. However, most weather stations do not include quantum sensors. As a result, there is considerable interest in modeling PPFD (Aguiar et al., 2011; Alados et al., 1996; Hu et al., 2007a; Xia et al., 2008), and it is often estimated from global shortwave irradiance (SW_i) measurements because pyranometers are common on weather stations. The modeling approach calculates PPFD from measured SW_i by multiplying by a factor that accounts for the fraction of PAR in SW_i (PAR/SW_i) and the average energy content of photons in the photosynthetically active range ($E_{Content}$):

$$PPFD_{Model} = SW_i \frac{PAR/SW_i}{E_{Content}} \qquad [16]$$

where PAR is in energy units of W m^{-2}, making the ratio PAR/SW_i unitless, and $E_{Content}$ is in units of J μmol^{-1}. Both PAR/SW_i and $E_{Content}$ are dependent on the solar spectrum, which varies with solar zenith angle and atmospheric conditions (e.g., degree of cloudiness, water vapor content). Solar spectral measurements made with a spectroradiometer (Advanced Spectral Designs model FieldSpec Pro) on a clear summer day in Logan, UT, yielded mean $E_{Content}$ of 0.221 J μmol^{-1} with approximately 1% variability for solar zenith angles less than 70°. Ross and Sulev (2000) reported a similar value, 0.219 J μmol^{-1}, for clear sky conditions. Akitsu et al. (2015) reported a mean value of 0.219 J μmol^{-1} with 3% variability. Spectral measurements on an overcast summer day in Logan, UT, yielded a value of 0.225 J μmol^{-1}.

Variability in PAR/SW_i for clear sky conditions was measured by rearranging Eq. [16] to solve for PAR/SW_i, inputting measured PPFD and SW_i from reference quantum sensors (mean of two Apogee model SQ-110, two Kipp & Zonen model PQS 1, and two LI-COR model LI-190 quantum sensors) and pyranometers (mean

of four secondary standard black-body thermopile pyranometers), and setting $E_{content}$ equal to 0.221 J μmol^{-1} (mean value for clear conditions). Results indicate a decline from about 0.45 at a solar zenith angle of 20° to 0.415 at a solar zenith angle of 80°, but scatter around the trendline is high (± 0.02) (Fig. 18), likely due to variable humidity in the atmosphere. A decline in SW_i/PAR with solar zenith angle is the expected trend based on spectral shifts of the solar spectrum. A greater proportion of shorter solar wavelengths (within PAR range) are filtered relative to longer solar wavelengths (outside PAR range) when the atmospheric path is long at high solar zenith angles.

Fig. 18. Solar zenith angle-dependent variability of the ratio of photosynthetically active radiation (PAR) to global shortwave irradiance (SW_i) on a horizontal surface for clear sky conditions in Logan, Utah, United States. Black line is a bin average. The ratio PAR/SW_i decreases as solar zenith angle increases due to increasing atmospheric air mass and greater filtering of wavelengths within the PAR range relative to those outside the PAR range.
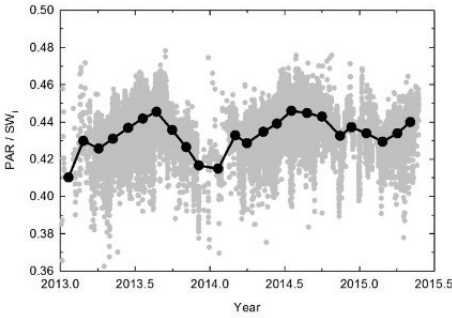
Fig. 19. Seasonal variability of the ratio of photosynthetically active radiation (PAR) to global shortwave irradiance (SW$_i$) on a horizontal surface for clear sky conditions in Logan, Utah, United States. Black line is a bin average. The ratio PAR/SW$_i$ decreased in winter months and increased in summer months due to seasonal changes in atmospheric air mass and water vapor content.
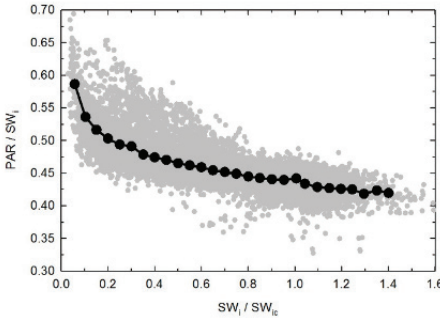
Fig. 20. Variability in the ratio of photosynthetically active radiation (PAR) to global shortwave irradiance (SW$_i$) with cloudiness (the ratio of SW$_i$ to clear sky global shortwave irradiance, SW$_{ic}$, is often called the cloudiness index and serves as a surrogate variable for cloudiness). Black line is a bin average. The ratio PAR/SW$_i$ increased as SW$_i$/SW$_{ic}$ decreased because clouds are more effective at filtering near infrared radiation than radiation within the PAR range.

Seasonal variability of PAR/SW$_i$ for clear sky conditions in Logan, UT, indicates a range of about 0.40 to 0.47, with low values occurring in winter and high values occurring in summer (Fig. 19), consistent with measurements from other locations (Alados et al., 1996; Hu et al., 2007b; Jacovides et al., 2007). Again, this is the expected trend based on spectral shifts of the solar spectrum. There is a greater proportion of red and near infrared radiation relative to blue radiation when solar zenith angle is relatively high during winter. The opposite occurs in summer. Water vapor content of the atmosphere likely influences seasonal trends as well because there is typically less water vapor in the atmosphere in winter and more in summer. A recent study also found a range of 0.40 to 0.47, with PAR/SW$_i$ increasing as atmospheric water vapor content increased (Akitsu et al., 2015), consistent with other studies (Bat-Oyun et al., 2012; Hu et al., 2007b; Weiss and Norman, 1985).

For all sky conditions, PAR/SW$_i$ increased as the sky transitioned from clear to cloudy (Fig. 20), consistent with the results from other studies (Escobedo et al., 2009; Jacovides et al., 2007). The mean value for clear sky conditions in Logan, UT, was 0.441, similar to that reported by others (Bat-Oyun et al., 2012; Jacovides et al., 2003; Meek et al., 1984; Weiss and Norman, 1985). Below a cloudiness index (SW$_i$/SW$_{ic}$) of about 0.3, PAR/SW$_i$ is greater than 0.50 (Fig. 20). Estimates of PAR/SW$_i$ can be derived from air mass and precipitable water (González and Calbó, 2002). Dust and aerosols can also have a large impact on PAR/SW$_i$ (Bat-Oyun et al., 2012; Jacovides et al., 2003).

Modeled PPFD, assuming a constant PAR/SW$_i$ = 0.45 (mean for all sky conditions) and constant $E_{Content}$ = 0.223 (mean of clear sky and overcast values), for two and a half years in Logan, UT, indicate deviation from measured PPFD (mean of value calculated from six reference quantum sensors) was typically less than 5%, unless

the sun was low in the sky (solar zenith angle greater than 60°) or sky was very cloudy ($SW_i/SW_{ic} < 0.3$). However, measurements from a quantum sensor over the same two and a half year period were much less variable and provided more accurate PPFD (Fig. 21). The simple model presented here (Eq. [16]) could be improved by accounting for solar zenith angle-dependent variability in PAR/SW_i for clear sky conditions (Fig. 18) and variability in PAR/SW_i with cloudiness (Fig. 20). However, scatter around trend lines in Fig. 18 and 20 indicates that even with these improvements, modeled PPFD likely won't be as accurate as measured PPFD.
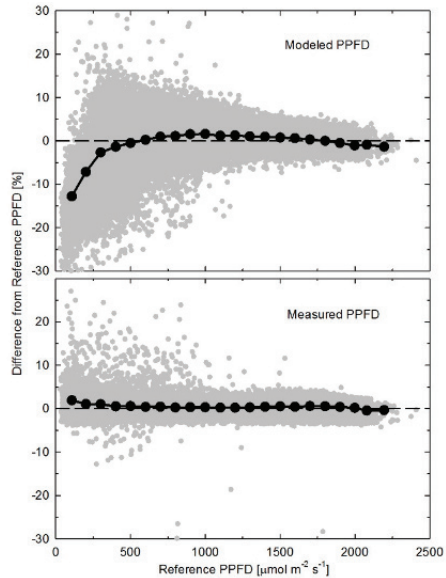

Fig. 21. Comparison of modeled (with Eq. [16]) and measured (with Apogee model SQ-110 quantum sensor) PPFD. Reference PPFD was mean calculated from six quantum sensors (two replicates each of Apogee Instruments model SQ-110, Kipp & Zonen model PQS 1, LI-COR model LI-190). Black lines are bin averages. Data were collected in Logan, UT, over a two and a half year time frame.

Summary

Radiation measurements are a key component on weather stations in agricultural weather and climate networks, and on flux towers. The radiation measurements made are dependent on the objectives of the measurement network and/or research site. At a minimum, global shortwave irradiance should be measured with a pyranometer. Silicon-cell pyranometers are often used for routine measurements, but thermopile pyranometers are more accurate for all sky conditions. For surface energy balance quantification, net radiation is required, with net radiation measurement from a four-component net radiometer typically being the most accurate method to obtain net radiation. Photosynthetically active radiation (PAR) is required in crop modeling and photosynthesis research. While PAR can be estimated from global shortwave irradiance measurements from a pyranometer, quantum sensors are more accurate and their use is becoming more common.

In addition to the information presented and reviewed in this chapter, the subjects of shortwave, net, and photosynthetically active radiation measurement have been treated extensively in the literature and this chapter is by no means exhaustive. For an excellent reference, particularly for shortwave and longwave irradiance measurements with pyranometers and pyrgeometers, respectively, see the recent book Solar and Infrared Radiation Measurements by Vignola et al. (2012).

References

Aguiar, L.J.G., G.R. Fischer, R.J. Ladle, A.C.M. Malhado, F.B. Justino, R.G. Aguiar, and J.M.N. da Costa. 2011. Modeling the photosynthetically active radiation in south west Amazonia under all sky conditions. Theor. Appl. Climatol. doi:10.1007/s00704-011-0556-z

Akitsu, T., A. Kume, Y. Hirose, O. Ijima, and K.N. Nasahara. 2015. On the stability of radiometric ratios of photosynthetically active radiation to global solar radiation in Tsukuba, Japan. Agric. For. Meteorol. 209-210:59–68. doi:10.1016/j.agrformet.2015.04.026

Alados, I., I. Foyo-Moreno, and L. Alados-Arboledas. 1996. Photosynthetically active radiation: Measurements and modeling. Agric. For. Meteorol. 78:121–131. doi:10.1016/0168-1923(95)02245-7

Alados-Arboledas, L., J. Vida, and J.I. Jiménez. 1988. Effects of solar radiation on the performance of pyrgeometers with silicon domes. J. Atmos. Ocean. Technol. 5:666–670. doi:10.1175/1520-0426(1988)005<0666:EOSROT>2.0.CO;2

Albrecht, B., and S.K. Cox. 1977. Procedures for improving pyrgeometer performance. J. Appl. Meteorol. 16:188–197. doi:10.1175/1520-0450(1977)016<0190:PFIPP>2.0.CO;2

Amiro, B.D., G.W. Thurtell, and T.J. Gillespie. 1983. A small infrared thermometer for measuring leaf temperature in leaf chambers. J. Exp. Bot. 34:1569–1576. doi:10.1093/jxb/34.11.1569

ASCE-EWRI. 2005. The ASCE standardized reference evapotranspiration equation. Report of the Task Committee on Standardization of Reference Evapotranspiration. Environmental and Water Resources Institute of the American Society of Civil Engineers, Reston, VA.

Atwater, M.A., and J.T. Ball, 1978. A numerical solar radiation model based on standard meteorological observations. Sol. Energy 21:163-170. doi:10.1016/0038-092X(78)90018-X

Baldridge, A.M., S.J. Hook, C.I. Grove, and G. Rivera. 2009. The ASTER spectral library version 2.0. Remote Sens. Environ. 113:711–715. doi:10.1016/j.rse.2008.11.007

Barnes, C., T. Tibbits, J. Sager, G. Deitzer, D. Bubenheim, G. Koerner, and B. Bugbee. 1993. Accuracy of quantum sensors measuring yield photon flux and photosynthetic photon flux. HortScience 28:1197–1200.

Bat-Oyun, T., M. Shinoda, and M. Tsubo. 2012. Effects of cloud, atmospheric water vapor, and dust on photosynthetically active radiation and total solar radiation in a Mongolian grassland. J. Arid Land 4:349–356. doi:10.3724/SP.J.1227.2012.00349

Beaubien, D.J., A. Bisberg, and A.F. Beaubien. 1998. Investigations in pyranometer design. J. Atmos. Ocean. Technol. 15:677–686. doi:10.1175/1520-0426(1998)015<0677:IIPD>2.0.CO;2

Biggs, W., A.R. Edison, J.D. Eastin, K.W. Brown, J.W. Maranville, and M.D. Clegg. 1971. Photosynthesis light sensor and meter. Ecology 52:125–131. doi:10.2307/1934743

Blonquist, J.M., Jr., B.D. Tanner, and B. Bugbee. 2009a. Evaluation of measurement accuracy and comparison of two new and three traditional net radiometers. Agric. For. Meteorol. 149:1709–1721. doi:10.1016/j.agrformet.2009.05.015

Blonquist, J.M., Jr., J.M. Norman, and B. Bugbee. 2009b. Automated measurement of canopy stomatal conductance based on infrared temperature. Agric. For. Meteorol. 149:1931–1945. doi:10.1016/j.agrformet.2009.06.021

Blonquist, J.M., Jr., R.G. Allen, and B. Bugbee. 2010. An evaluation of the net radiation sub-model in the ASCE standardized reference evapotranspiration equation: Implications for evapotranspiration prediction. Agric. Water Manage. 97:1026–1038. doi:10.1016/j.agwat.2010.02.008

Brotzge, J.A., and C.E. Duchon. 2000. A field comparison among a domeless net radiometer, two four-component net radiometers, and a domed net radiometer. J. Atmos. Ocean. Technol. 17:1569–1582. doi:10.1175/1520-0426(2000)017<1569:AFCAAD>2.0.CO;2

Campbell, G.S., and G.R. Diak. 2005. Net and thermal radiation estimation and measurement. In: J.L. Hatfield and J.M. Baker, editors, Micrometeorology in Agricultural Systems. ASA, Madison, WI. p. 59–92.

Campbell, G.S., and J.M. Norman. 1998. An introduction to environmental biophysics. Springer-Verlag, New York. doi:10.1007/978-1-4612-1626-1

Campbell, G.S., J.N. Mugaas, and J.R. King. 1978. Measurement of long-wave radiant flux in organismal energy budgets: A comparison of three methods. Ecology 59:1277–1281. doi:10.2307/1938242

Cobos, D.R., and J.M. Baker. 2003. Evaluation and modification of a domeless net radiometer. Agron. J. 95:177–183. doi:10.2134/agronj2003.0177

Duchon, C.E., and G.E. Wilk. 1994. Field comparisons of direct and component measurements of net radiation under clear skies. J. Appl. Meteorol. 33:245–251. doi:10.1175/1520-0450(1994)033<0245:FCODAC>2.0.CO;2

Dutton, E.G., J.J. Michalsky, T. Stoffel, B.W. Forgan, J. Hickey, D.W. Nelson, T.L. Alberta, and I. Reda. 2001. Measurement of broadband diffuse solar irradiance using current commercial instrumentation with a correction for thermal offset errors. J. Atmos. Ocean. Technol. 18:297–314. doi:10.1175/1520-0426(2001)018<0297:MOBDSI>2.0.CO;2

Enz, J.W., J.C. Klink, and D.G. Baker. 1975. Solar radiation effects on pyrgeometer performance. J. Appl. Meteorol. 14:1297–1302. doi:10.1175/1520-0450(1975)014<1297:SREOPP>2.0.CO;2

Escobedo, J.F., E.N. Gomes, A.P. Oliveira, and J. Soares. 2009. Modeling hourly and daily fractions of UV, PAR, and NIR to global solar radiation under various sky conditions at Botucatu, Brazil. Appl. Energy 86:299–309. doi:10.1016/j.apenergy.2008.04.013

Fairall, C.W., P.O.G. Persson, E.F. Bradley, R.E. Payne, and S.P. Anderson. 1998. A new look at calibration and use of Eppley precision infrared radiometers. Part I: Theory and application. J. Atmos. Ocean. Technol. 15:1229–1242. doi:10.1175/1520-0426(1998)015<1229:ANLACA>2.0.CO;2

Federer, C.A., and C.B. Tanner. 1965. A simple integrating pyranometer for measuring daily solar radiation. J. Geophys. Res. 70:2301–2306. doi:10.1029/JZ070i010p02301

Federer, C.A., and C.B. Tanner. 1966. Sensors for measuring light available for photosynthesis. Ecology 47:654–657. doi:10.2307/1933948

Field, R.T., L.J. Fritschen, E.T. Kanemasu, E.A. Smith, J.B. Stewart, S.B. Verma, and W.P. Kustas. 1992. Calibration, comparison, and correction of net radiation instruments used during FIFE. J. Geophys. Res. 97:18,681–18,695. doi:10.1029/91JD03171

Flerchinger, G.N., W. Xaio, D. Marks, T.J. Sauer, and Q. Yu. 2009. Comparison of algorithms for incoming atmospheric longwave radiation. Water Resour. Res. 45:W03423. doi:10.1029/2008WR007394

Foken, T. 2008. The energy balance closure problem– An overview. Ecol. Appl. 18:1351–1367. doi:10.1890/06-0922.1

Fritschen, L.J., and C.L. Fritschen. 2007. Calibration of shielded net radiometers. Agron. J. 99:297–303. doi:10.2134/agronj2005.0077s

Fuchs, M., and C.B. Tanner. 1966. Infrared thermometry of vegetation. Agron. J. 58:597–601. doi:10.2134/agronj1966.00021962005800060014x

Geuder, N., R. Affolter, B. Kraas, and S. Wilbert. 2014. Long-term behavior, accuracy and drift of LI-200 pyranometers as radiation sensors in Rotating Shadowband Irradiometers (RSI). Energy Procedia 49:2330–2339. doi:10.1016/j.egypro.2014.03.247

González, J.A., and J. Calbó. 2002. Modelled and measured ratio of PAR to global radiation under cloudless skies. Agric. For. Meteorol. 110:319–325. doi:10.1016/S0168-1923(01)00291-X

Gröbner, J., and A. Los. 2007. Laboratory calibration of pyrgeometers with known spectral responsivities. Appl. Opt. 46:7419–7425. doi:10.1364/AO.46.007419

Gueymard, C.A. 2008. REST2: High-performance solar radiation model for cloudless-sky irradiance, illuminance, and photosynthetically active radiation– Validation with a benchmark dataset. Sol. Energy 82:272–285. doi:10.1016/j.solener.2007.04.008

Gueymard, C.A. 2012. Clear-sky irradiance predictions for solar resource mapping and large-scale applications: Improved validation methodology and performance analysis of 18 broadband radiative models. Sol. Energy 86:2145–2169. doi:10.1016/j.solener.2011.11.011

Habte, A., S. Wilcox, and T. Stoffel. 2014. Evaluation of radiometers deployed at the National Renewable Energy Laboratory's Solar Radiation Research Laboratory. Technical Report NREL/TP-5D00-60896. National Renewable Energy Laboratory, Golden, CO.

Haeffelin, M., S. Kato, A.M. Smith, C.K. Rutledge, T.P. Charlock, and J.R. Mahan. 2001. Determination of the thermal offset of the Eppley precision spectral pyranometer. Appl. Opt. 40:472–484. doi:10.1364/AO.40.000472

Halldin, S., and A. Lindroth. 1992. Errors in net radiometry: Comparison and evaluation of six radiometer designs. J. Atmos. Ocean. Technol. 9:762–783. doi:10.1175/1520-0426(1992)009<0762:EINRCA>2.0.CO;2

Hu, B., Y. Wang, and G. Liu. 2007a. Measurements and estimations of photosynthetically active radiation in Beijing. Atmos. Res. 85:361–371. doi:10.1016/j.atmosres.2007.02.005

Hu, B., Y. Wang, and G. Liu. 2007b. Spatiotemporal characteristics of photosynthetically active radiation in China. J. Geophys. Res. 112:1–12. doi:10.1029/2006JD007965

Huband, N.D.S. 1985a. An infra-red radiometer for measuring surface temperature in the field. Part I. Design and Construction. Agric. For. Meteorol. 34:215–226. doi:10.1016/0168-1923(85)90021-8

Huband, N.D.S. 1985b. An infra-red radiometer for measuring surface temperature in the field Part II. Calibration and performance. Agric. For. Meteorol. 34:227–233. doi:10.1016/0168-1923(85)90022-X

Idso, S.B. 1981. A set of equations for full spectrum and 8- to 14-μm and 10.5- to 12.5-μm thermal radiation from cloudless skies. Water Resour. Res. 17:295–304. doi:10.1029/WR017i002p00295

Inada, K. 1976. Action spectra for photosynthesis in higher plants. Plant Cell Physiol. 17:355–365.

Jacovides, C.P., F.S. Tymvios, D.N. Asimakopoulos, K.M. Theofilou, and S. Pashiardes. 2003. Global photosynthetically active radiation and its relationship with global solar radiation in the Eastern Mediterranean basin. Theor. Appl. Climatol. 74:227–233. doi:10.1007/s00704-002-0685-5

Jacovides, C.P., F.S. Tymvios, V.D. Assimakopoulos, and N.A. Kaltsounides. 2007. The dependence of global and diffuse PAR radiation components on sky conditions at Athens, Greece. Agric. For. Meteorol. 143:277–287. doi:10.1016/j.agrformet.2007.01.004

JCGM/WG 1, 2008. Guide to the expression of uncertainty in measurement. Working Group 1 of the Joint Committee for Guides in Metrology. http://www.bipm.org/utils/common/documents/jcgm/JCGM_100_2008_E.pdf (verified 17 July 2016).

Ji, Q., and S.-C. Tsay. 2000. On the dome effect of Eppley pyrgeometers and pyranometers. Geophys. Res. Lett. 27:971–974. doi:10.1029/1999GL011093

Ji, Q., and S.-C. Tsay. 2010. A novel nonintrusive method to resolve the thermal dome effect of pyranometers: Instrumentation and observational basis. J. Geophys. Res. doi:10.1029/2009JD013483

Kalma, J.D., H. Alksnis, and G.P. Laughlin. 1988. Calibration of small infra-red surface temperature transducers. Agric. For. Meteorol. 43:83–98. doi:10.1016/0168-1923(88)90008-1

Kerr, J.P., G.W. Thurtell, and C.B. Tanner. 1967. An integrating pyranometer for climatological observer stations and mesoscale networks. J. Appl. Meteorol. 6:688–694. doi:10.1175/1520-0450(1967)006<0688:AIPFCO>2.0.CO;2

Kimball, B.A., S.B. Idso, and J.K. Aase. 1982. A model of thermal radiation from partly cloudy and overcast skies. Water Resour. Res. 18:931–936. doi:10.1029/WR018i004p00931

King, D.L., and D.R. Myers. 1997. Silicon-photodiode pyranometers: Operational characteristics, historical experiences, and new calibration procedures. In: Proceedings from the 26th IEEE Photovoltaic Specialists Conference, 29 Sept.–3 Oct. 1997, Anaheim, CA. IEEE, New York. doi:10.1109/PVSC.1997.654323

King, D.L., J.A. Kratochvil, and W.E. Boyson. 1997. Measuring solar and spectral angle-of-incidence effects on photovoltaic modules and solar irradiance sensors. In: Proceedings from the 26th IEEE Photovoltaic Specialists Conference, Sept. 29-Oct. 3, 1997, Anaheim, CA. IEEE, New York, New York. doi:10.1109/PVSC.1997.654283

Klassen, S., and B. Bugbee. 2005. Shortwave Radiation. In: J.L. Hatfield and J.M. Baker, editors, Micrometeorology in agricultural systems. ASA, Madison, WI. p. 43–57.

Kopp, G., and J.L. Lean. 2011. A new, lower value of total solar irradiance: Evidence and climate significance. Geophys. Res. Lett. 38:1–7. doi:10.1029/2010GL045777

Kohsiek, W., C. Liebethal, T. Foken, R. Vogt, S.P. Oncley, C. Bernhofer, and H.A.R. Debruin. 2007. The energy balance experiment EBEX-2000. Part III: Behaviour and quality of the radiation measurements. Boundary-Layer Meteorol. 123:55–75. doi:10.1007/s10546-006-9135-8

Kustas, W.P., J.H. Prueger, L.E. Hipps, J.L. Hatfield, and D. Meek. 1998. Inconsistencies in net radiation estimates from use of several models of instruments in a desert environment. Agric. For. Meteorol. 90:257–263. doi:10.1016/S0168-1923(98)00062-8

Lefèvre, M., A. Oumbe, P. Blanc, B. Espinar, B. Gschwind, Z. Qu, L. Wald, M. Schroedter-Homscheidt, C. Hoyer-Klick, A. Arola, A. Benedetti, J.W. Kaiser, and J.-J. Morcrette. 2013. McClear: A new model estimating downwelling solar radiation at ground level in clear-sky conditions. Atmos. Meas. Tech. 6:2403–2418. doi:10.5194/amt-6-2403-2013

Leuning, R., E. van Gorsel, W.J. Massman, and P.R. Isaac. 2012. Reflections on the surface energy imbalance problem. Agric. For. Meteorol. 156:65–74. doi:10.1016/j.agrformet.2011.12.002

Malek, E. 2008. The daily and annual effects of dew, frost, and snow on a non-ventilated net radiometer. Atmos. Res. 89:243–251. doi:10.1016/j.atmosres.2008.02.006

Marty, C., R. Philipona, J. Delamere, E.G. Dutton, J. Michalsky, K. Stamnes, R. Storvold, T. Stoffel, S.A. Clough, and E.J. Mlawer. 2003. Downward longwave irradiance uncertainty under arctic atmospheres: Measurements and modeling. J. Geophys. Res. 108:4358–4369. doi:10.1029/2002JD002937

McCree, K.J. 1972a. The action spectrum, absorptance and quantum yield of photosynthesis in crop plants. Agric. Meteorol. 9:191–216. doi:10.1016/0002-1571(71)90022-7

McCree, K.J. 1972b. Test of current definitions of photosynthetically active radiation against leaf photosynthesis data. Agric. Meteorol. 10:443–453. doi:10.1016/0002-1571(72)90045-3

Meek, D.W., J.L. Hatfield, T.A. Howell, S.B. Idso, and R.J. Reginato. 1984. A generalized relationship between photosynthetically active radiation and solar radiation. Agron. J. 76:939–945. doi:10.2134/agronj1984.00021962007600060018x

Meloni, D., C. Di Biagio, A. Di Sarra, F. Monteleone, G. Pace, and H.M. Sferlazzo. 2012. Accounting for the solar radiation influence on downward longware irradiance measurements by pyrgeometers. J. Atmos. Ocean. Technol. 29:1629–1643. doi:10.1175/JTECH-D-11-00216.1

Menyhart, L., A. Anda, and Z. Nagy. 2015. A new method for checking the leveling of pyranometers. Sol. Energy 120:25–34. doi:10.1016/j.solener.2015.06.033

Meyers, T.P., and R.F. Dale. 1983. Predicting daily insolation with hourly cloud height and coverage. J. Clim. Appl. Meteorol. 22:537–545. doi:10.1175/1520-0450(1983)022<0537:PDIWHC>2.0.CO;2

Michalsky, J., E. Dutton, M. Rubes, D. Nelson, T. Stoffel, M. Wesley, M. Splitt, and J. DeLuisi. 1999. Optimal measurement of surface shortwave irradiance using current instrumentation. J. Atmos. Ocean. Technol. 16:55–69. doi:10.1175/1520-0426(1999)016<0055:OMOSSI>2.0.CO;2

Michel, D., R. Philipona, C. Ruckstuhl, R. Vogt, and L. Vuilleumier. 2008. Performance and uncertainty of CNR 1 net radiometers during a one-year field comparison. J. Atmos. Ocean. Technol. 25:442–451. doi:10.1175/2007JTECHA973.1

Mims, F.M., III. 2003. A 5-year study of a new kind of photosynthetically active radiation sensor. Photochem. Photobiol. 77:30–33. doi:10.1562/0031-8655(2003)077<0030:AYSOAN>2.0.CO;2

Miskolczi, F., and R. Guzzi. 1993. Effect of nonuniform spectral dome transmittance on the accuracy of infrared radiation measurements using shielded pyrradiometers and pyrgeometers. Appl. Opt. 32:3257–3265. doi:10.1364/AO.32.003257

Myers, D.R. 2011. Quantitative analysis of spectral impacts on silicon photodiode radiometers. NREL/CP-5500-50936. National Renewable Energy Laboratory Conference Paper, Golden, CO.

Myers, D.R. 2013. Solar radiation practical modeling for renewable energy applications. CRC Press, Taylor & Francis Group, Boca Raton, FL.

Norman, J.M., and F. Becker. 1995. Terminology in thermal infrared remote sensing of natural surfaces. Agric. For. Meteorol. 77:153–166. doi:10.1016/0168-1923(95)02259-Z

Ohmura, A., E.G. Dutton, B. Forgan, C. Fröhlich, H. Gilgen, H. Hegner, A. Heimo, G. König-Langlo, B. McArthur, G. Müller, R. Philipona, R. Pinker, C.H. Whitlock, K. Dehne, and M. Wild. 1998. Baseline surface radiation network ()BSRN/WCRP): New precision radiometry for climate research. Bull. Am. Meteorol. Soc. 79:2115–2136. doi:10.1175/1520-0477(1998)079<2115:BSRNBW>2.0.CO;2

Oliveira, A.P., J. Soares, M.Z. Božnar, P. Mlakar, and J. Escobedo. 2006. An application of neural network technique to correct the dome temperature effects on pyrgeometer measurements. J. Atmos. Ocean. Technol. 23:80–89. doi:10.1175/JTECH1829.1

Osterwald, C.R. 1986. Translation of device performance measurements to reference conditions. Sol. Cells 18:269–279. doi:10.1016/0379-6787(86)90126-2

Pérez, M., and L. Alados-Arboledas. 1999. Effects of natural ventilation and solar radiation on the performance of pyrgeometers. J. Atmos. Ocean. Technol. 16:174–180. doi:10.1175/1520-0426(1999)016<0174:EONVAS>2.0.CO;2

Philipona, R. 2002. Underestimation of solar global and diffuse radiation measured at Earth's surface. J. Geophys. Res. doi:10.1029/2002JD002396

Philipona, R., C. Fröhlich, and C. Betz. 1995. Characterization of pyrgeometers and the accuracy of atmospheric longwave radiation measurements. Appl. Opt. 34:1598–1605. doi:10.1364/AO.34.001598

Philipona, R., C. Fröhlich, K. Dehne, J. DeLuisi, J. Augustine, E. Dutton, D. Nelson, B. Forgan, P. Novotny, J. Hickey, S.P. Love, S. Bender, B. McArthur, A. Ohmura, J.H. Seymour, J.S. Foot, M. Shiobara, F.P.J. Valero, and A.W. Strawa. 1998. The baseline surface radiation network pyrgeometer round-robin calibration experiment. J. Atmos. Ocean. Technol. 15:687–696. doi:10.1175/1520-0426(1998)015<0687:TBSRNP>2.0.CO;2

Philipona, R., E.G. Dutton, T. Stoffel, J. Michalsky, I. Reda, A. Stifter, P. Wendling, N. Wood, S.A. Clough, E.J. Mlawer, G. Anderson, H.E. Revercomb, and T.R. Shippert. 2001. Atmospheric longwave irradiance uncertainty: Pyrgeometers compared to an absolute sky-scanning radiometer, atmospheric emitted radiance interferometer, and radiation transfer model calculations. J. Geophys. Res. 106:28129–28141.

Pontailler, J.-Y. 1990. A cheap quantum sensor using a gallium arsenide photodiode. Funct. Ecol. 4:591–596. doi:10.2307/2389327

Raïch, A., J.A. González, and J. Calbó. 2007. Effects of solar height, cloudiness and temperature on silicon pyranometer measurements. Tethys 4:11–18. doi:10.3369/tethys.2007.4.02

Reda, I., J. Hickey, C. Long, D. Myers, T. Stoffel, S. Wilcox, J.J. Michalsky, E.G. Dutton, and D. Nelson. 2005. Using a blackbody to calculate net longwave responsivity of shortwave solar pyranometers to correct for their thermal offset error during outdoor calibration using the component sum method. J. Atmos. Ocean. Technol. 22:1531–1540. doi:10.1175/JTECH1782.1

Reda, I. 2011. Method to calculate uncertainties in measuring shortwave solar irradiance using thermopile and semiconductor solar radiometers. Technical Report NREL/TP-3B10-52194. National Renewable Energy Laboratory, Golden, CO. doi:10.2172/1021250

Riihimaki, L., and F. Vignola. 2008. Establishing a consistent calibration record for Eppley PSPs. In: Proceedings of the 37th American Solar Energy Society Conference, San Diego, CA. 3–8 May 2008. American Solar Energy Society, Boulder, CO.

Ross, J., and M. Sulev. 2000. Sources of errors in measurements of PAR. Agric. For. Meteorol. 100:103–125. doi:10.1016/S0168-1923(99)00144-6

Sager, J.C., W.O. Smith, J.L. Edwards, and K.L. Cyr. 1988. Photosynthetic efficiency and phytochrome photoequilibria determination using spectral data. Trans. ASAE 31:1882–1889. doi:10.13031/2013.30952

Selcuk, K., and J.I. Yellott. 1962. Measurement of direct, diffuse and total solar radiation with silicon photovoltaic cells. Sol. Energy 6:155–163. doi:10.1016/0038-092X(62)90127-5

Sengupta, M., P. Gotseff, D. Myers, and T. Stoffel. 2012. Performance testing using silicon devices– Analysis and accuracy. Conference Paper NREL/CP-5500-54251. National Renewable Energy Laboratory, Golden, CO. doi:10.1109/PVSC.2012.6318278

Steinhilber, F., J. Beer, and C. Fröhlich. 2009. Total solar irradiance during the Holocene. Geophys. Res. Lett. 36:L19704. doi:10.1029/2009GL040142

Tanner, B.D. 2001. Evolution of automated weather station technology through the 1980s and 1990s. In: K.G. Hubbard and M.V.K. Sivakumar, editors, Automated weather stations for applications in agriculture and water resources management: Current uses and future perspectives. WMO/TD number 1074. World Meteorological Organization, Geneva, Switzerland. p. 3–20.

Twine, T.E., W.P. Kustas, J.M. Norman, D.R. Cook, P.R. Houser, T.P. Meyers, J.H. Prueger, P.J. Starks, and M.L. Wesely. 2000. Correcting eddy-covariance flux underestimates over a grassland. Agric. For. Meteorol. 103:279–300. doi:10.1016/S0168-1923(00)00123-4

Udo, S.O. 2000. Quantification of solar heating of the dome of a pyrgeometer for a tropical location: Ilorin, Nigeria. J. Atmos. Ocean. Technol. 17:995–1000. doi:10.1175/1520-0426(2000)017<0995:QOSHOT>2.0.CO;2

Unsworth, M.H., and J.L. Monteith. 1975. Long-wave radiation at the ground: I. Angular distribution of incoming radiation. Q. J. R. Meteorol. Soc. 101:1029–1030. doi:10.1002/qj.49710143029

Vieira, L.E.A., S.K. Solanki, N.A. Krivova, and I. Usoskin. 2011. Evolution of the solar irradiance during the Holocene. Astron. Astrophys. 531:A6–A26. doi:10.1051/0004-6361/201015843

Vignola, F., J. Michalsky, and T. Stoffel. 2012. Solar and infrared radiation measurements. CRC Press, Taylor & Francis, Boca Raton, FL.

Weiss, A., and J.M. Norman. 1985. Partitioning solar radiation into direct and diffuse, visible and near-infrared components. Agric. For. Meteorol. 34:205–213. doi:10.1016/0168-1923(85)90020-6

Wilson, K.B. 2002. Energy balance closure at FLUXNET sites. Agric. For. Meteorol. 113:223–243. doi:10.1016/S0168-1923(02)00109-0

Wood, J.D., T.J. Griffis, and J.M. Baker. 2015. Detecting drift bias and exposure errors in solar and photosynthetically active radiation data. Agric. For. Meteorol. 206:33–44. doi:10.1016/j.agrformet.2015.02.015

Xia, X., Z. Li, P. Wang, M. Cribb, H. Chen, and Y. Zhao. 2008. Analysis of photosynthetic photon flux density and its parameterization in northern China. Agric. For. Meteorol. 148:1101–1108. doi:10.1016/j.agrformet.2008.02.008

Yordanov, G.H., O.-M. Midtgård, T.O. Saetre, H.K. Nielsen, and L.E. Norum. 2012. Overirradiance (cloud enhancement) events at high latitudes. In: Photovoltaic Specialists Conference, Vol. 2, Austin, TX. 3–8 June 2012 IEEE, New York. doi: 10.1109/PVSC-Vol 2.2013.6656797